Marine Pollution Bulletin 225 (2026) 119266

Contents lists available at ScienceDirect

Marine Pollution Bulletin

journal homepage: www.elsevier.com/locate/marpolbul

A spectrally-derived method for detecting sea-water discoloration around submarine volcanoes in oligotrophic oceans by integrating Sentinel 2 A/B-MSI and Landsat 8/9-OLI data

Emanuele Ciancia [a,b,*], Francesco Marchese [a,b], Giuseppe Mazzeo [a,b], Simon Plank [c], Nicola Pergola [a,b]

[a] *Institute of Methodologies for Environmental Analysis, Italian National Research Council, Tito Scalo, Pz, Italy*
[b] *Space Technologies and Applications Centre, Potenza, Italy*
[c] *German Remote Sensing Data Center, German Aerospace Center (DLR), Oberpfaffenhofen, Germany*

ARTICLE INFO

Keywords:
Remote sensing
Multi-sensor data
Sea-water discoloration
Submarine volcanoes
Oligotrophic waters

ABSTRACT

Shallow eruptions of submarine volcanoes can hamper navigation of ships and alter the biological response of marine ecosystems. Satellite remote sensing can provide timely and continuous information about volcanic activity around dangerous sites contributing to the assessment of pre-, syn- and post eruptive phenomena. Among these, sea-water discoloration is one of the most significant indicators of underwater volcanic activity as its accurate and timely detection may help in revealing possible precursor processes of submarine volcanic eruptions. In this framework, we proposed a novel spectrally-derived method to detect and map discolored plumes around submarine volcanoes in oligotrophic oceans by integrating Sentinel 2A/B-MSI and Landsat 8/9-OLI satellite data. The developed method, combining two discoloration algorithms, was tested around a representative test case, namely the Kavachi Volcano (Solomon Islands, Southwest Pacific Ocean), by using a yearly (2022) MSI-OLI integrated dataset. It exhibited satisfactory validation metrics thus recording overall accuracies (OAs) close to 90% for both the single and integrated (multi-sensor) configuration. Despite the omission errors ranging (OEs) from 18 to 20%, the very low (around 2%) commission (CEs) demonstrated its high level of reliability in mapping discolored waters of volcanic origin. Furthermore, the proven exportability of this method to the Kaitoku Volcano (Japan, Western Pacific Ocean) confirms its capability in detecting underwater volcanic activities regardless of different features of sea-water discoloration (e.g., chemical composition). This method could represent an automated early warning tool to support the operational monitoring of submarine volcanoes arranged by maritime surveillance systems.

1. Introduction

Most volcanic eruptions on Earth (around 80%) occur in the oligotrophic oceans in both convergent and divergent plate margins (Mitchell, 2012; Urai, 2014). Although most underwater eruptions are deep enough to be unknown or undetected (O'Malley et al., 2014; Tepp and Dziak, 2021), shallow eruptions have been widely investigated as they can hamper navigation of ships and alter the biological responses of marine ecosystems (González-Vega et al., 2020; Sakuno, 2021). Hydrothermal plumes, discolored waters and ongoing venting materials can occur for weeks affecting the optical properties of the water column (Baker et al., 2012). Submarine eruptions are usually recorded and monitored by subaerial displays (Baker et al., 2002), fortuitous underwater observations (Rubin et al., 2012), deployments of hydro-acoustic (Dziak et al., 2011) or seismic arrays (Schlindwein et al., 2005). However, most of these methods are usually time-consuming, expensive and can be difficult to perform close to an eruption (Barone et al., 2022; Fraile-Nuez et al., 2012; Sakuno et al., 2023). Furthermore, they are generally used when eruptions have begun, and volcanic products have already spread on sea-surface thus preventing the investigation of the pre-eruptive volcanic processes (Green et al., 2013).

Satellite remote sensing may provide timely and continuous information on volcanic activity around hazardous locations enabling pre-, syn- and post-eruptive phenomena to be recognized (Eugenio et al.,

---

* Corresponding author at: Institute of Methodologies for Environmental Analysis, Italian National Research Council, Tito Scalo, Pz, Italy.
E-mail address: emanuele.ciancia@cnr.it (E. Ciancia).

https://doi.org/10.1016/j.marpolbul.2026.119266
Received 13 May 2025; Received in revised form 8 January 2026; Accepted 8 January 2026

2014; Sakuno et al., 2023; Falconieri et al., 2025; Plank et al., 2025).

Among them, sea-water discoloration is one of the most significant indicators of underwater volcanic activity (Mantas et al., 2011; Urai and Machida, 2005) as its timely detection can provide advance warning of submarine volcanic eruptions (Sakuno et al., 2023).

Several studies were performed to investigate and track discolored water plumes through the assessment of their colors (Sakuno, 2021; Sakuno et al., 2023), chemical compositions and reflectance patterns by using Ocean Colour (OC) data (Coca et al., 2014; Mantas et al., 2011; Urai and Machida, 2005). Urai and Machida (2005) exploited the Advanced Spaceborn Thermal Emission and Reflection Radiometer (ASTER) reflectance products to investigate sea-water discoloration due to the Satsuma-Iwojima (Japan) submarine eruption, discriminating two shades of discolored water. Other works demonstrated the suitability of Moderate Resolution Imaging Spectroradiometer (MODIS) reflectance data in identifying discolored water types, with differences in terms of spatial distribution and spectral features during submarine eruptions in the Southwest Pacific Ocean (Mantas et al., 2011; Shi and Wang, 2011). Shi and Wang (2011) analyzed reflectance spectra of an ash-laden patch after the Tonga volcanic eruption in 2009, discovering unique optical features which differ from those of clear, productive, and turbid waters.

Subsequent studies combined reflectance pattern analyses with satellite retrievals of different optical parameters, such as downwelling diffuse attenuation coefficient at 490 nm (k_d 490), chlorophyll-a concentration (chl-a), particulate back-scattering coefficient ($b_{bp}(\lambda)$) and/or physical variables like sea surface temperature (SST) (Coca et al., 2014; Eugenio et al., 2014; O'Malley et al., 2014). Coca et al. (2014) developed a classification scheme based on MODIS-derived k_d 490 and reflectance ratios to investigate the spatio-temporal dynamics of submarine volcanic plumes at the island El Hierro (Canary Islands). O'Malley et al. (2014) developed a Level 3 (L3) MODIS-based index for detecting submarine volcanic eruptions by seeking infrequent increases in chl-a and $b_{bp}(\lambda)$ following each event.

The most recent studies highlighted the need to integrate multi-sensor and multispectral OC data acquired by MODIS, Visible Infrared Imaging Radiometer Suite (VIIRS) and Sentinel-3 Ocean and Land Color Instrument (OLCI) (Whiteside et al., 2021) to better estimate timing and duration of submarine eruptions and characterize discolored patches in terms of extent and suspended matter volume (Whiteside et al., 2023; Kelly et al., 2024). The above-mentioned sensors were mostly used to detect discolored plumes after huge eruptions (e.g., Hunga Tonga-Hunga Ha'apai Volcano in January 2022) thanks to their wide spatial coverage and high revisiting time. However, their coarse spatial resolution makes them unsuitable for accurately mapping pumice rafts (Jutzeler et al., 2020; Chen et al., 2022; Zheng et al., 2022; Fauria et al., 2023) or sea-water discoloration drifting from submarine volcanoes (Caballero et al., 2022). Since most discolored patches have small dimensions, irregular and elongate shapes, higher resolution satellite data are required to better detect and accurately map their spatial features that are at approximately ten- or hundred-meter scale (Caballero et al., 2022; Fauria et al., 2023; Urai and Machida, 2005). The improved spatial resolution of the Operational Land Imager (OLI) and Multi-Spectral Instrument (MSI), onboard the Landsat 8/9 (L8/9-OLI) and Sentinel-2A/B (S2A/B-MSI) satellite platforms provide significant opportunities to detect spatial heterogeneity of aquatic environments, although both MSI and OLI were initially designed for terrestrial applications (Ciancia et al., 2020; Page et al., 2019; Pahlevan et al., 2019). Furthermore, the combined use of these multi-platform sensors can allow sea-water discoloration to be monitored at rates that have never been possible before because of their improved temporal coverage at 10–60 m spatial resolution (Caballero et al., 2022).

This study aims to evaluate the potential of integrated S2A/B-MSI and L8/9-OLI observations in characterizing sea-water discoloration originating from submarine volcanoes. The submarine Kavachi Volcano (Solomon Islands, South Pacific Ocean) is used as a representative test case since observations of the discolored water plumes were intermittently reported from October 2021 (Global Volcanism Program, 2021). In this context, the key objectives of this work are to: (1) derive the spectral features of discolored sea-water around Kavachi using a yearly (2022) MSI-OLI integrated dataset and (2) develop a semi-automated method for MSI and OLI data capable of detecting and mapping discolored plumes around submarine volcanoes in oligotrophic oceans.

2. Data

2.1. Study area

Kavachi is one of the most active volcanoes in the Solomon Islands arc in the Southwest Pacific Ocean (Phillips et al., 2016). It is located south of Gatokae and Vangunu Islands (within the New Georgia Island Group) 30 km northeast of the convergent boundary, where the Australian plate subducts beneath the Pacific plate (Fig. 1b). Kavachi (8°59′37″S, 157°58′21″E) is a submarine volcano that is also characterized by phreatomagmatic (explosive water-magma interactions) and occasional subaerial eruptions that form ephemeral islands; these eruptions eject steam, ash and incandescent bombs (Phillips et al., 2016).

From 1939 to 1991, several eruptive periods were recorded, with ephemeral islands forming in, for example, 1970, 1976, 1978 and 1991 (Global Volcanism Program, 1976, 1978, 1991). The most recent eruptions occurred in 2000, 2004 and 2014 when observers from research vessels reported conspicuous discolored plumes, ejected ash and incandescent lava blocks that reached heights of about 70 m above the sea surface (Global Volcanism Program, 2000, 2005, 2017). During these years summit of Kavachi was in a constant state of flux, as eruptions continuously formed islands that were soon eroded away (Phillips et al., 2016).

Based on independent in-situ bathymetric measurements by Philips et al., 2016, the summit has a shallow oblong crater that measures approximately 120 m × 75 m and rises to an average depth of 24 m below sea level (b.s.l.). Kavachi has a conical shape characterized by almost uniform flanks with 18° slopes that descend to depths >1000 m b.s.l. (Phillips et al., 2016). In this work, due to the lack of in-situ measurements, the bathymetry of the area around Kavachi (Fig. 1c) was obtained from the Global Multi-Resolution Topography (GMRT) base map (Ryan et al., 2009). To ensure a continuous bathymetric layer, the “gdal_fillnodata” algorithm (available in the Quantum Geographic Information System (QGIS)) was used to interpolate and fill data gaps where high-resolution detail was unavailable.

From an oceanographic point of view, the study area shows oligotrophic conditions and typical characteristics of the West Pacific Warm Pool (WPWP) with warm surface waters (annual sea surface temperature > 28 °C), thick mixed layer and a deep thermocline (~200 m) (Bali et al., 2020; Baker et al., 2002).

2.2. Satellite data

To identify and map sea-water discoloration around submarine volcanoes both S2A/B-MSI and L8/9-OLI data were analyzed to create an integrated dataset of analysis. The S2A/B-MSI platforms ensure a 5-day revisit time (at the equator) in paired operations delivering optical data in 13 bands in the 440–2200 nm spectral range with a 10–60 m spatial resolution. L8/9-OLI provides multispectral imagery in 9 bands in the same spectral domain, with a 30 m spatial resolution enabling up to 8-day revisit frequency in the combined mode (Table 1).

In addition, PlanetScope-SuperDove8 (PS-SD8) data were exploited with the aim of performing a cross-checking validation procedure. PlanetScope is a constellation of approximately 130 commercial satellites designed for imaging the Earth's land surface and coastal waters every day at meter scale resolution (Planet Developer Center, 2024). PS-SD8 is the third-generation sensor acquiring optical imagery in 8 bands

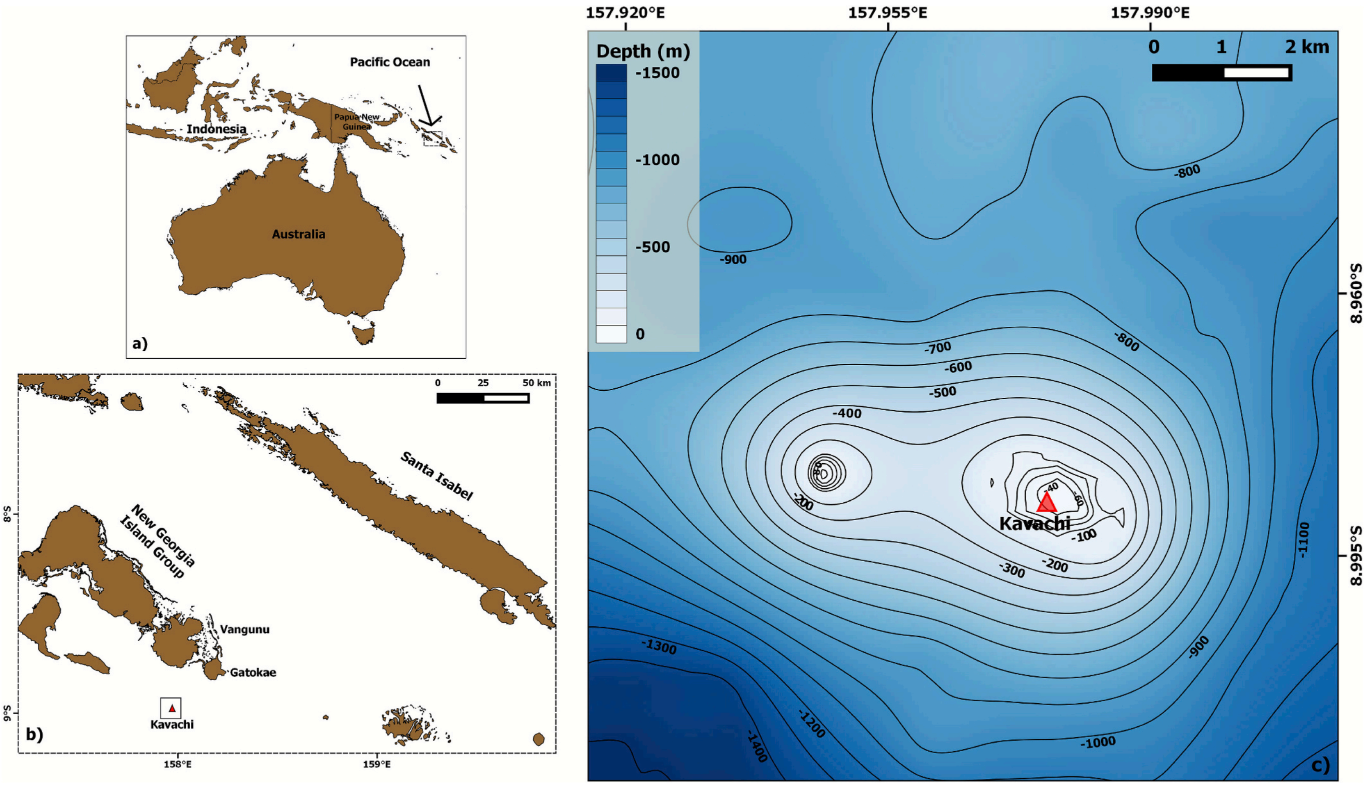

Fig. 1. Study area. a) Large map of the Oceania region showing the Solomon Islands. Box and arrow define area shown in b). b) Map of the Santa Isabel Island and the New Georgia Island Group in the Solomon Islands showing position of the Kavachi Volcano. Box defines area shown in c). c) Bathymetry of the study area around the Kavachi Volcano. The bathymetric data was obtained from the Global Multi-Resolution Topography (GMRT) base map (Ryan et al., 2009) with GeoMapApp (GeoMapApp tool, 2009).

Table 1
Central wavelength [nm] and (spatial resolution [m]) of the S2A/B-MSI, L8/9-OLI and PS-SD8 bands used in this work.

Sensor	Blue1	Blue2	Green	Red	NIR	SWIR1	SWIR2
MSI	443 (60)	492 (10)	560 (10)	665 (10)	865 (10)	1614 (20)	2202 (20)
OLI	443 (30)	483 (30)	561 (30)	655 (30)	865 (30)	1609 (30)	2201 (30)
SD8	444 (3)	492 (3)	566 (3)	666 (3)	866 (3)	–	–

in the 444–866 nm spectral domain with a 3 m spatial resolution (Table 1) (Vanhellemont, 2023).

In this work, the OLI Level-1T (L1T) and MSI Level-1C (L1C) data (geo-located and radiometrically calibrated top of atmosphere (TOA) reflectance) were provided by the United States Geological Survey (USGS) web portal (USGS Web Portal, 2024) and the Copernicus browser (Copernicus browser, 2024), respectively. All the OLI-L1T and MSI-L1C tiles covering the Kavachi Volcano subset (Fig. 1c) from 2022 were downloaded. After excluding imagery affected by over 50% cloud cover, straylight effects and sea roughness, a total of 30 images were processed, 15 for L8/9-OLI (089 Path – 066 Row, 23:36 UTC acquisition time) and 15 for S2A/B-MSI (T57LUL granule, 23:49 UTC acquisition time).

Concerning the PS-SD8 data, only the satellite image of 14 May 2022 was processed and retained for the cross-checking validation. In detail, the eight-band imagery was obtained as orthorectified TOA radiances (TOAR, bundle name anlytic_8b_udm2) with 3 × 3 m pixel size from the Planet Explorer website (Planet Developer Center, 2024).

2.2.1. *Atmospheric correction and data processing*

We processed satellite data to retrieve the atmospherically corrected remote sensing reflectance Level 2 (L2) Rrs(λ). These are the input variables of the spectrally-derived method for detecting sea-water discoloration.

All the Level-1 (L1C, L1T and TOA) data were processed to L2 Rrs(λ) using the ACOLITE toolbox (version 20220222) (ACOLITE software, 2024), a free software specifically developed to support processing of meter-scale satellite data in aquatic applications (Satriano et al., 2024; Ciancia et al., 2023).

Within the ACOLITE software, the multi-band "Dark Spectrum Fitting" (DSF) algorithm (Vanhellemont and Ruddick, 2018) was implemented to perform the atmospheric correction chain. The DSF inherent rationale is to dynamically select the reference "dark band" on which the atmospheric path reflectance (ρ_{path}) is determined and assumed constant over the tile of interest (Vanhellemont, 2019). DSF uses the acquired TOA reflectance (ρ_t) over dark targets (with sea surface reflectance $\rho_s \approx 0$) in the scene or subscene to derive a "dark spectrum" (ρ_{dark}) and compute the aerosol optical depth (τ_a at 550 nm) for each band in this dark spectrum (Vanhellemont, 2020). To identify the most appropriate aerosol model, DSF selects the one minimizing the difference between ρ_{dark} and ρ_{path} in the two bands with the lowest τ_a estimation. After selecting τ_a and the aerosol model, all the required atmospheric parameters, namely ρ_{path}, two-way total transmittance (T_d and T_u) and the spherical albedo of the atmosphere (S) are derived from a lookup table (LUT). Considering a uniform Lambertian target, surface reflectance, $\rho_s(\lambda)$ or Rrs(λ) (i.e., obtained as ρ_s/π) can be estimated from ρ_t, as:

$$\frac{\rho_t}{T_g} = \rho_{path} + \frac{\rho_s{}^{*}T_dT_u}{1-\rho_s{}^{*}S} \tag{1}$$

where T_g is the band average gas transmittance, estimated by adopting variable concentrations of water vapour and ozone (Vanhellemont, 2023). Within a first processing phase, pixels with high ρ_t in the SWIR2 or NIR bands were discarded to avoid false identifications of land or clouds. To this aim, a site-tuned filtering of non-water pixels was applied using fixed thresholds in the SWIR2 band for S2A/B-MSI and L8/9-OLI data ($\rho_t > 0.06$) and in the NIR one ($\rho_t > 0.05$) for PS-SD8. Negative $\rho_s(\lambda)$ values were also removed to exclude data affected by issues in the atmospheric correction (overestimation of atmospheric reflectance) or the satellite imagery itself.

To further account for sunglint contamination, a semi-automated correction was implemented on the imagery acquired within the austral spring-summer period. In detail, a SWIR1-based threshold approach (pixels with $\rho_s < 0.11$ were subjected to glint correction) was performed only on the S2A/B-MSI and L8/9-OLI data due to the lack of the SWIR bands within the PS-SD8 spectral configuration.

Finally, the S2/B-MSI and L8/9-OLI Rrs(λ) were generated at 30 m spatial resolution after resampling the S2A/B-MSI Rrs(λ) (nominal spatial resolution of 10–60 m) by the nearest neighbor method. On the contrary, PS-SD8 Rrs(λ) were processed and retained at their native spatial resolution (3 m).

3. Method

3.1. Generation of the reference Rrs(λ)

Developing a spectrally derived method for detecting sea-water discoloration requires a preliminary analysis to define the reference Rrs(λ) of clear and discolored oceanic waters. Starting from direct visual inspections of S2A/B-MSI and L8/9-OLI imagery we identified reference discolored/clear waters using band combinations in true colors.

Among all the reported observations of sea-water discoloration originating from Kavachi (Global Volcanism Program, 2022; Global Volcanism Program, 2023b), we examined a total of 20 RGB (Red, Green, Blue2) images during 2022, including ten for S2A/B-MSI and ten for L8/9-OLI. For each image, we randomly selected three locations

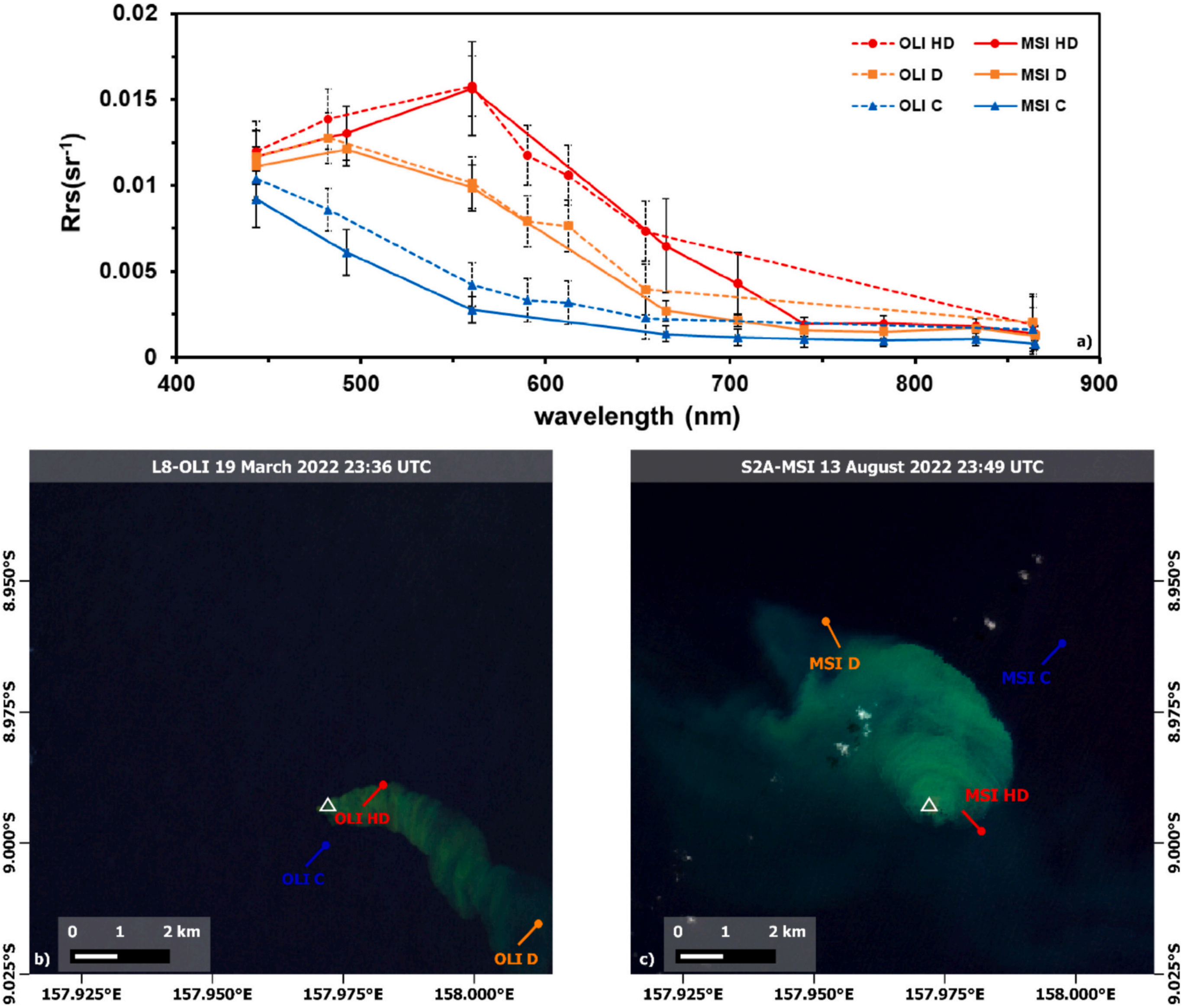

Fig. 2. Reference Rrs(λ). a) Rrs(λ) averages derived from the 20 images (i.e., ten for S2A/B-MSI and ten for L8/9-OLI) for each water type considered (i.e., C, D, HD). Rrs(λ) standard deviations are the black continuous (for S2A/B-MSI) and dashed (for L8/9-OLI) bars, respectively. b,c) Example of a random selection of three pins related to clear (C), discolored (D) and highly discolored (HD) waters on the RGB images of L8-OLI (19 March 2022) and S2A-MSI (13 August 2022) resampled at 30 m spatial resolution. The location of Kavachi is depicted by the white triangle.

showing conditions of clear, discolored and highly discolored waters to compute Rrs(λ) average for each condition, with distinction between S2A/B-MSI and L8/9-OLI data. In Fig. 2a the major spectral discrepancies are between clear waters and the two discolored classes (e.g., discolored and highly discolored). The average Rrs(λ) values of clear waters show the typical shape of oligotrophic oceanic waters with a peak in the Blue1 band and decreasing values at increasing wavelengths. On the contrary, discolored waters display the opposite spectral pattern (increasing phase) compared with the clear ones in the Blue1-Green spectral domain. Discolored waters exhibit a reflectance peak shifting from Blue2 to Green for increasing discoloration levels usually detected closest to the volcano. There are no appreciable differences in the Rrs(λ) averages between S2A/B-MSI and L8/9-OLI data. However, the Rrs(λ) average values of L8/9-OLI are slightly higher than those of S2A/B-MSI, especially in the Blue1-Green spectral range (Fig. 2c).

3.2. *Comparison between S2A/B-MSI and L8/9-OLI in the Green band*

The spectral comparison between S2A/B-MSI and L8/9-OLI served as the basis to assess their integrated use. An image-based MSI-OLI comparison in a specific band was performed with the aim of setting a common spectral threshold on both S2A/B-MSI and L8/9-OLI for detecting discolored waters of volcanic origin. For this purpose, we compared the MSI and OLI Rrs(λ) data in the Green band (see Table 1) because it has the highest spectral sensitivity to ash-laden discolored waters (Sakuno et al., 2023). Within the year of analysis, we selected that date characterized by near-simultaneous (time difference < 15 min) overpasses between S2A/B-MSI and L8/9-OLI to assume similar aerosol/

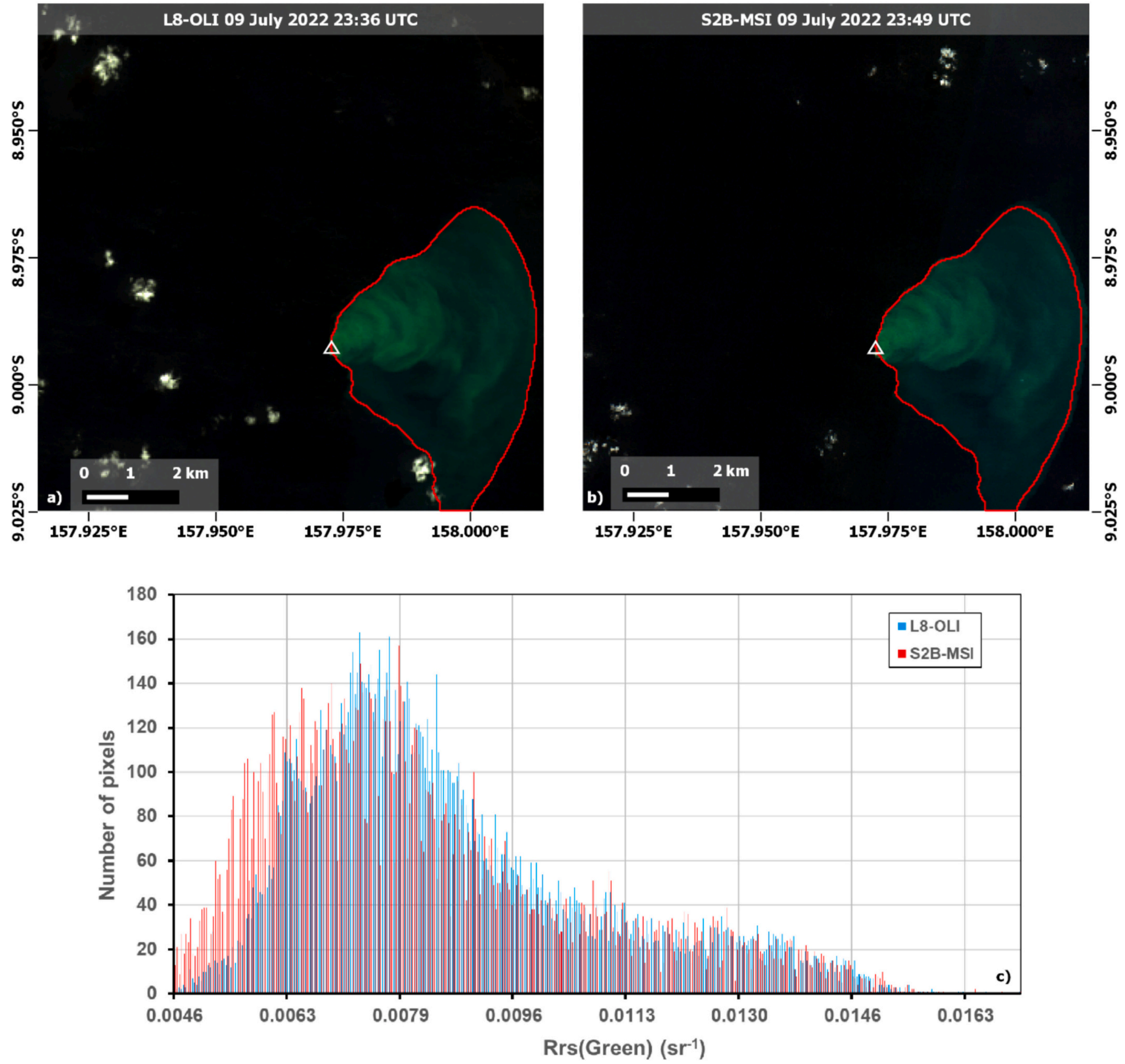

Fig. 3. MSI-OLI intercomparison. a,b) L8-OLI (23:36 UTC) and S2B-MSI (23:49 UTC) images of 9 July 2022 in true colors at 30 m spatial resolution. The continuous red line delimits the RGB-derived discolored area around the Kavachi Volcano depicted by the white triangle. c) Frequency histograms of Rrs(Green) over the discolored area detected in the panels (a-b). (For interpretation of the references to color in this figure legend, the reader is referred to the web version of this article.)

atmospheric conditions and ensure a more accurate comparison.

We compared the corresponding Rrs(λ) values in the Green band over the common discolored area for the S2B-MSI and L8-OLI acquisitions on 9 July 2022. The continuous red line in Fig. 3a-b encloses the common RGB-based discolored area for images acquired 13-min apart on 9 July 2022. The S2B-MSI and L8-OLI frequency histograms exhibit similar Rrs(Green) fluctuations (Fig. 3c) over such a discolored area. The median Rrs(Green) values differ by ~5% (equal to 0.0004 sr^{-1} absolute difference) between L8-OLI and S2B-MSI with absolute values of 0.0082 and 0.0078 sr^{-1}, respectively.

3.3. Definition of discoloration algorithms

The spectral analyses (3.1 and 3.2 sections) defined the most suitable spectral tests and thresholds for the development of discoloration detection algorithms. In this work, we proposed two configurations of discoloration algorithms, namely the Spectrally Derived Discoloration (SDD) and the Spectrally-Derived High Discoloration (SDHD), to detect pixels with different intensity of discoloration around submarine volcanoes in oligotrophic waters. Concerning SDD, pixels are detected as discolored if all the three spectral tests used are true, namely "Blue ratio", "Green Threshold" and "Red NIR", as follows:

- *The "Blue ratio" spectral test*: in oligotrophic clear waters the maximum Rrs(λ) is observed at 412–443 nm (i.e., Blue1) and decreases at increasing wavelengths (Hu et al., 2012; Mélin et al., 2016), while for moderate discolored waters Rrs(λ) peak shifts from 443 to 490 nm (i.e., Blue2) (Coca et al., 2014). Therefore, discolored pixels should be detected if:

$$\frac{Rrs(Blue1)}{Rrs(Blue2)} < 1 \tag{2}$$

- *The "Green Threshold" spectral test*: the Green band usually records the highest Rrs values in areas of discolored waters compared with normal ocean conditions (Whiteside et al., 2023). The common threshold value for S2A/B-MSI and L8/9-OLI was cautiously set below the average Rrs(Green) values of discolored pixels (Fig. 2c) and the median Rrs(Green) values observed within the frequency histograms of Section 3.2 (Fig. 3c). Discolored pixels should be detected if:

$$Rrs(Green) > 0.0075\ sr^{-1} \tag{3}$$

- *The "Red-NIR" spectral test*: the rationale is to avoid potential detections of massive blooms of floating algae (e.g., Green *Noctiluca scintillans*, Trichodesmium or Microcystis species) whose Rrs(λ) display the typical red-edge shape within the Red-NIR range (Gernez et al., 2023; Spyrakos et al., 2018; Qi et al., 2020). Hence, discolored pixels should be detected if:

$$\frac{Rrs(Red)}{Rrs(NIR)} > 1 \tag{4}$$

Concerning the SDHD configuration, the first and third spectral tests are unchanged while the "Green Threshold" is replaced by the following one:

- *The "Blue-Green ratio" spectral test*: as turbidity increases Rrs(λ) values display a rising shape in the Blue1–Green range with a peak at about 560 nm (Di Polito et al., 2016; Doxaran et al., 2002; Jiang et al., 2021; Jiang et al., 2023). Highly discolored pixels should be detected if:

$$\frac{Rrs(Blue2)}{Rrs(Green)} < 1 \tag{5}$$

Also, for SDHD, pixels are detected as highly discolored if the "Blue ratio", "Blue-Green ratio" and "Red-edge" spectral tests are all true. Fig. 4 displays the flowchart for detecting discolored or highly discolored pixels from S2A/B-MSI and L8/9-OLI imagery through the adoption of the SDD and SDHD algorithms, respectively. For each algorithm configuration (SDD or SDHD) we generated a binary map where discolored or highly discolored pixels were set to 1, while other water pixels were set to 0.

The Sentinel Application Platform (SNAP) was used to implement the discoloration algorithms and QGIS software packages for complementary elaborations.

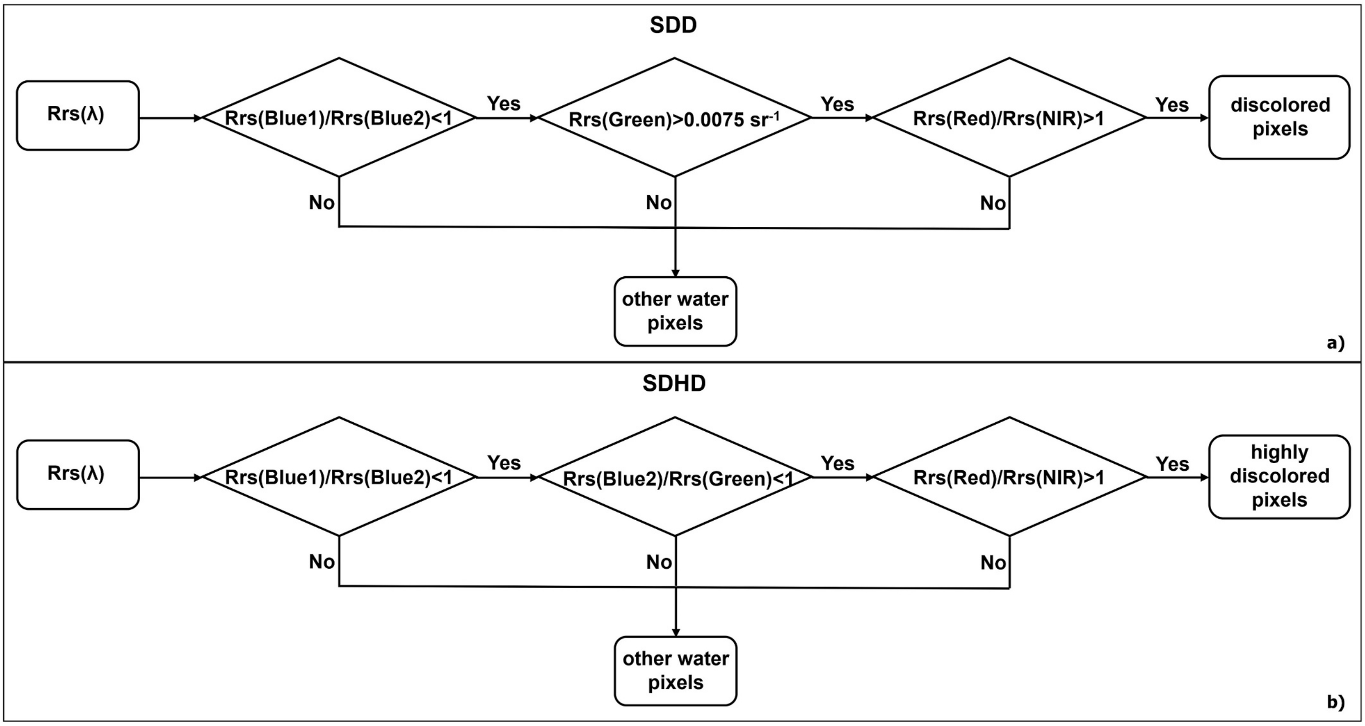

Fig. 4. SDD and SDHD algorithms. Flowcharts of the SDD (a) and SDHD (b) algorithms implemented on both the S2A/B-MSI and L8/9-OLI Rrs(λ) data.

3.4. Validation procedure and accuracy metrics

Establishing if a satellite pixel is truly discolored is not a simple task, especially if there are no direct field observations. According to a widely accepted practice (Chen et al., 2022; Coluzzi et al., 2018; Coluzzi et al., 2025; Jutzeler et al., 2020), we determined the pixels representing the "sea-truth" by applying a manual method based on visual inspections of true-color (i.e., RGB) images under the supervision of a trained expert. Considering for validation the remaining images (five for S2A/B-MSI and five L8/9-OLI images) of the whole dataset, we, firstly, generated, for each image, the RGB-derived reference mask setting binary values of 1 and 0 for discolored and other water pixels, respectively. Based on the binary maps obtained from the SDD and SDHD algorithms, we derived a per-image discolored mask. Discolored pixels detected by at least one of the two algorithms were assigned the value of 1, while other water pixels identified by both (i.e., SDD and SDHD) were assigned the value of 0. These discolored masks were then superimposed with the corresponding reference ones to obtain the validation maps and determine the confusion matrices (error matrices).

The validation maps that were generated display agreement and disagreement areas classified into the four categories of the confusion matrix. These are: a) True Positive (TP), i.e., agreements between discolored pixels), b) True Negative (TN), i.e., agreements between other water pixels, c) False Positive (FP), i.e., disagreements between other water pixels/discolored pixels (other water pixels in the reference mask, discolored pixels in the algorithm-derived one), d) False Negative (FN), i.e., disagreements between discolored/other water pixels (discolored pixels in the reference mask, other water pixels in the algorithm-derived one). From the confusion matrix, we computed the commission and omission errors, the overall accuracy and the Cohen's Kappa (K) coefficient.

The commission error (CE) describes the percentage of discolored pixels falsely classified in the algorithm-derived mask (overestimation) and can be defined as:

$$CE(\%) = 100 - \left(\frac{TP}{TP + FP}\right)*100 \tag{6}$$

The omission error (OE) is the percentage of discolored pixels in the RGB-derived reference mask that have been omitted in the algorithm-based one (underestimation), and it can be written as:

$$OE(\%) = 100 - \left(\frac{TP}{TP + FN}\right)*100 \tag{7}$$

The overall accuracy (OA) represents a similar estimation between the two masks, and it can be defined as:

$$OA(\%) = \left[\frac{(TP + TN)}{(TP + FN + TN + FP)}\right]*100 \tag{8}$$

K (Congalton, 1991) provides a more realistic indication about the probability that a pixel is correctly classified by including off-diagonal elements of the error matrix. K ranges between 0 and 1 with higher values indicating a closer agreement between the reference and the algorithm-derived masks. It can be written as:

$$K = \frac{2*(TP*TN - FN*FP)}{(TP + FP)*(FP + TN) + (TP + FN)*(FN + TN)} \tag{9}$$

To estimate accuracy metrics, we did not perform statistics for every image to avoid oversampling issues. The number of other water pixels per image is significantly higher than the number of discolored ones thus determining an excessive predominance of potential TNs over the scene and consequently a less indicative OA for the algorithm performance. To overcome this limitation, we randomly selected from all available ten images, a total of 10,000 "true" pixels (i.e., 5000 for S2A/B-MSI and 5000 for L8/9-OLI imagery) equally split into truly discolored (50%) and truly other water pixels (50%), following the approach of Chen et al. (2022).

4. Results

4.1. General performance of the SDD/SDHD algorithms

As a first step, we evaluated the performance of the proposed discoloration algorithms by visually comparing the RGB-based images with the corresponding SDD/SDHD derived maps. Fig. 5 shows these maps for six test dates (the remaining four are reported in Fig. S1) for which discolored plumes drifting from the Kavachi Volcano were independently reported (Global Volcanism Program, 2022, 2023a). The selected test cases are characterized by variable acquisition conditions and discolored plumes with differences in terms of extension and color shades.

Discolored areas identified by the SDD and SDHD algorithms generally superimpose the visible yellow-green patches on the true color imagery. The SDHD algorithm detects the plume core that usually represents the most discolored area closest to the volcano (Fig. 5b′, c′, d′, e′). The SDD algorithm identifies larger and less discolored areas up to 4–5 km far from Kavachi, as shown in Fig. 5b′, f′. In some cases, the areas identified by the SDD and SDHD algorithms tend to completely overlap probably because of high discoloration level occurring at satellite acquisition time. On 19 February 2022 (Fig. 5 a, a′), both the algorithms identify most of the eastward dispersed plume with an 80% overlap between the SDHD and SDD-derived areas. On other test dates, the occurrence of underwater volcanic activity well before the satellite overpass causes the SDHD algorithm to identify fewer discolored pixels because of the plume attenuation. This leads to a significant decrease of this overlap, with the lowest value (~32%) being on 3 September 2022 (Fig. 5 f′). However, SDD sometimes may (partially) fail to detect the most distal part of the plumes, for example, the northern greenish patch on 14 May 2022 (Fig. 5e′). Furthermore, most of the undetected pixels by SDD are located on the transition (buffer) zone between discolored plume core and clear waters, as on 21 March 2022 (Fig. 5 b′) and 20 April 2022 (Fig. 5 c′, d′). On 20 April 2022 discolored areas exhibited identical features between the near-simultaneous acquisitions (<15 min) of L8-OLI and S2B-MSI (Fig. 5 c, c′, d, d′) data. In both acquisitions SDHD mainly detects a plume drifting southward (with a slightly higher sensitivity from L8-OLI data; see red pixels) while the SDD also identifies a westward branch that is less discolored. With a more quantitative analysis, the SDD-detected areas range between 5.44 and 5.38 km^2 while the SDHD-detected areas are between 4.16 and 3.6 km^2 for L8-OLI and S2B-MSI, respectively.

Despite a slight difference between the corresponding SDHD-detected areas, the results confirm the inter-operability of the proposed algorithms regardless of the satellite-sensor system employed.

4.2. Accuracy assessment of the discoloration algorithm

Regarding the accuracy analysis, we considered a single discoloration algorithm (with a binary discolored/no discolored classifier) including both the SDD and SDHD configurations, as described in Section 3.4. Performance of the algorithm-derived discoloration masks was evaluated through validation maps showing agreement and disagreement areas labeled into four categories of error matrices (i.e., TP, TN, FP, FN). Fig. 6 displays validation maps for four representative test dates (the remaining six are reported in Fig. S2) under different performance conditions.

Among the considered test cases in Fig. 6, the L9-OLI acquisition of 28 April 2022 shows the largest fraction of correctly discolored pixels (red), together with the smallest fraction of undetected ones (black). Furthermore, the agreement between discolored pixels (red) is observable also close to the less visible discolored patch at about 5 km northwest from the volcano (Fig. 6b, b′). Sometimes, the correct classification of discolored pixels occurs in the core of plumes and is lacking at their

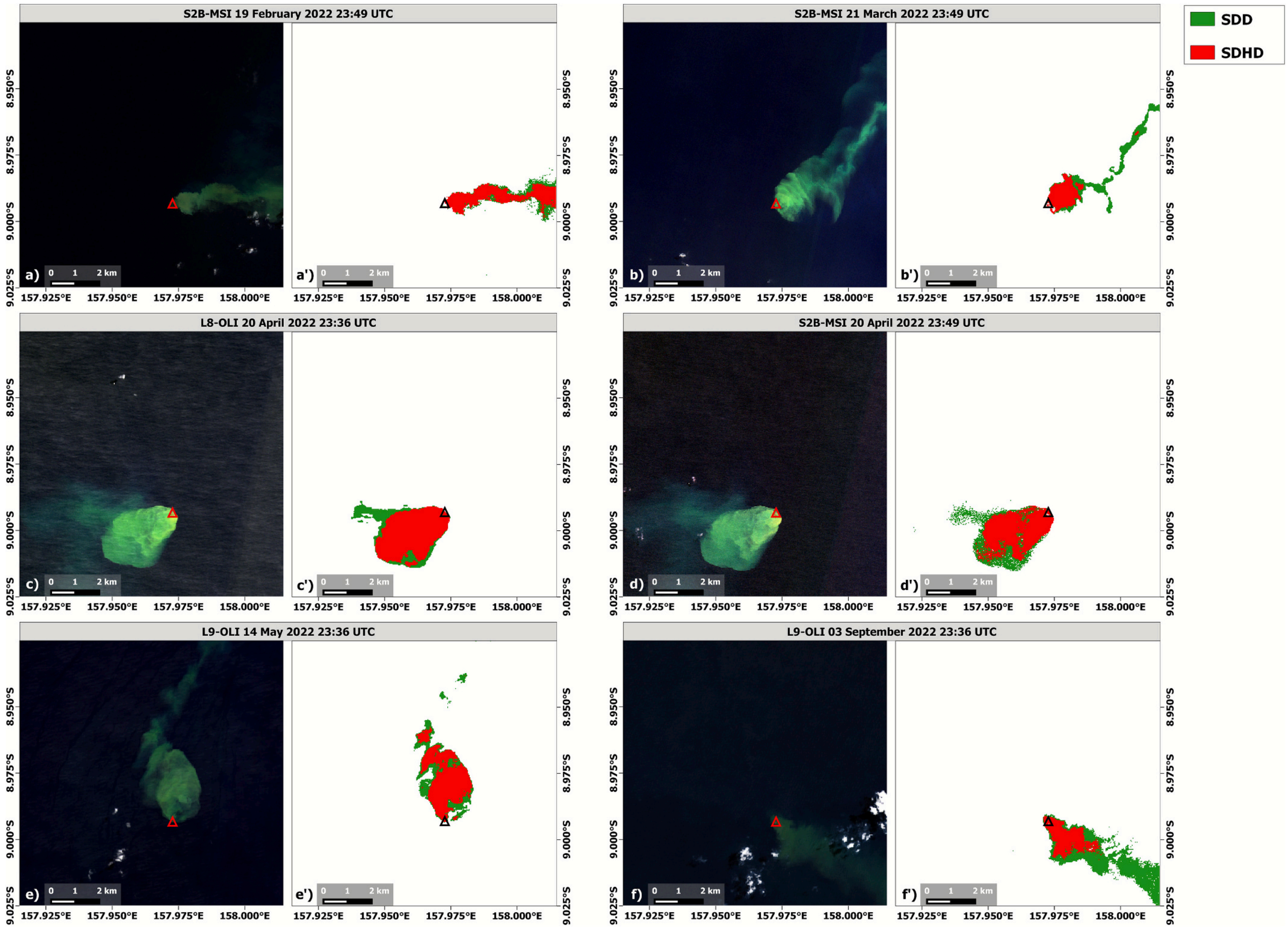

Fig. 5. Discoloration maps by the SDD/SDHD algorithms. S2A/B-MSI and L8/9-OLI imagery in true color composite (Red, Green, Blue2) for the selected test dates (a, b, c, d, e, f). Discoloration maps derived by the SDD (green) and SDHD (red) algorithms for the corresponding test dates (a′, b′, c′, d′, e′, f′). The white pixels on the discoloration maps represent the discarded ones, namely cloudy/no data or other water pixels. The location of Kavachi is shown by the red and black triangles in the (a–f) and (a′–f′) panels, respectively. (For interpretation of the references to color in this figure legend, the reader is referred to the web version of this article.)

edges, as shown in Fig. 6 a′, c′. In these cases, the fraction of truly discolored pixels overlaps just with the most visible greenish plume in the true-color imagery (Fig. 6 a, c). The portion of the undetected pixels characterizes the transition zone between the plume core and the clear water conditions where the discoloration effects tend to be smoothed. However, underestimation can also result along the plume core if the sea-surface conditions are not spatially homogeneous, as on 14 November 2022. It is likely that the occurrence of sea-surface roughness determines the fragmentation of the discolored patches with relative discontinuities between truly discolored and undetected pixels over the greenish plume (Fig. 6 f′).

Table 2 summarizes the error metrics computed over all ten images of the validation dataset, according to the procedure described in Section 3.4. Statistics are reported with distinction between S2A/B-MSI (i.e., five images and 5000 pixels) and L8–9/OLI (i.e., five images and 5000 pixels) data and considering an integrated multi-sensor dataset (i.e., ten images and 10,000 pixels).

Table 2 shows the good performance of the discoloration algorithm considering both the single and the integrated (multi-sensor) configuration. Although statistics related to L8/9-OLI data are slightly better than S2A/B-MSI, in all cases the error metrics are satisfactory thus exhibiting OAs close to 90%, CEs not exceeding 1% and K values always around 0.8. However, the higher OEs (approximately 18%) confirm the tendency for the algorithm to underestimate the truly discolored pixels especially over the buffer zones around the plume core, as shown in Fig. 6 a′. Conversely, the significantly low CEs certify the algorithm reliability highlighted by the negligible number of false detections.

4.3. Cross-checking for validation by PlanetScope data

Considering the lack of in-situ data for the validation analysis, we performed a cross-checking procedure by assuming the PS-SD8 data as “ground truth”, exploiting its very high (i.e., 3 m) spatial resolution. For this purpose, we used 14 May 2022 as the test date, because it was the only one characterized by near-simultaneous (time difference of 15 min) overpasses between L9-OLI and PS-SD8. After upsampling the L9-OLI Rrs(λ) data to 3 m spatial resolution by the nearest neighbor method, we obtained the algorithm-derived binary mask (discolored/no discolored classifier). This mask was then superimposed with the RGB reference one of PS-SD8 to obtain the validation map and error matrices. Fig. 7 displays the comparison between the PS-SD8 RGB image and the corresponding L9-OLI validation map for 14 May 2022 along with a spectral analysis of specific selected areas. Fig. 7c shows the Rrs(λ) averages over three 5×5-pixel boxes (randomly selected) centered on the correctly discolored areas, the undetected ones, and the clear water conditions.

Fig. 7 shows that the portion of correctly classified pixels (in red) concerns not only the most visible green plume but also some slightly

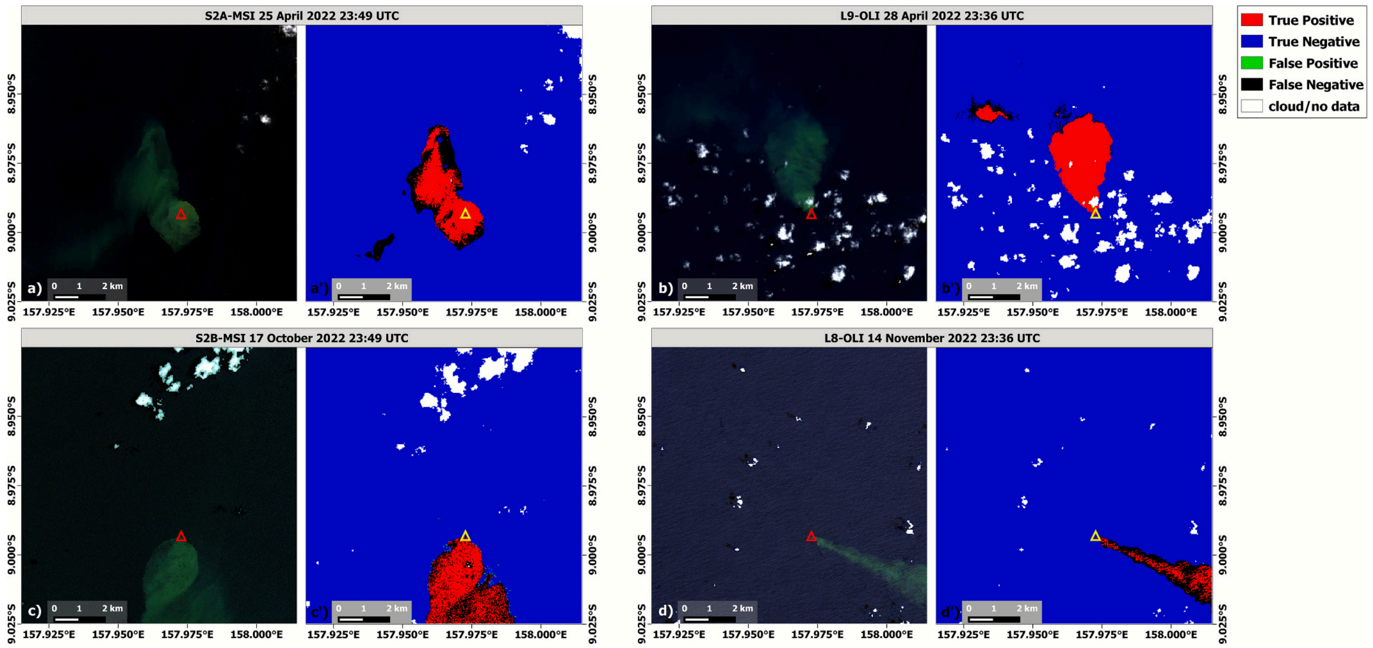

Fig. 6. Validation maps. S2A/B-MSI and L8/9-OLI imagery in true color composite (Red, Green, Blue2) of the selected test dates (a, b, c, d). Validation maps of the corresponding test dates (a′, b′, c′, d′). Validation maps highlight agreement between discolored pixels, TP (red), agreement between other water pixels, TN (blue), disagreements between other water pixels/discolored pixels, FP (green), and between disagreements discolored/other water pixels, FN (black). The location of Kavachi is defined by the red and yellow triangles in the (a–d) and (a′–d′) panels, respectively. (For interpretation of the references to color in this figure legend, the reader is referred to the web version of this article.)

Table 2
Accuracy metrics of the algorithm-derived discoloration masks. CE commission error (overestimation), OE omission error (underestimation), OA overall accuracy and K Cohen's Kappa coefficient.

Satellite-sensor system	CE (%)	OE (%)	OA (%)	K
S2A/B-MSI	0.84	19.85	89.73	0.80
L8/9-OLI	1.06	17.84	90.64	0.81
S2A/B-MSI & L8/9-OLI	0.95	18.84	90.19	0.80

less discolored branches, which are in the middle-west part of the image. Conversely, the missed detections (in black) characterize mostly the transition zone between discolored and clear waters, where the intensity contrast between these sea-surface features is not particularly evident in the RGB image. Although the false detections (in green) are relatively low, they are confined to the eastern edge of the plume core and are likely due to errors in the upsampling procedure of the L9-OLI data.

Table 3 summarizes the error metrics computed considering all the pixels of the image given the lower occurrence of TNs.

The statistics shown in Table 3 agree with those of the previous analysis (Table 2), confirming the good performance of the discoloration algorithm. Values of OA (90.43%) and K (0.80) are satisfactory and almost the same as before, while CE records a slight increase up to 2.16% due to some FPs located on the eastern edge of the plume. Also in this case, the lack of true detections in the buffer zones determines an OE of approximately 21%, slightly higher than the computed value over the five images of the L8/9-OLI validation dataset (Table 2). This value confirms that the algorithm slightly underestimates both the less discolored and the most distal parts of the plumes due to the failure of the "Green Threshold" spectral test. The spectral analysis (Fig. 7c) clearly shows that the Rrs(Green) average for the undetected area (B2 UD in Fig. 7) is below the threshold value of 0.0075 sr^{-1}.

4.4. Evaluation of the algorithm exportability

An accurate assessment of the performance of discoloration algorithms over different geographic areas and test sites is crucial to evaluate their potential in providing information about underwater activity of other volcanoes. Therefore, we also examined a documented episode of sea-water discoloration occurring around the Kaitoku Volcano (with two primary peaks at an average depth of 95 m b.s.l.) located in the Izu-Ogasawara arc (Northwest Pacific Ocean) about 1000 km south of Tokyo (Japan) (Fig. 8a). Among the various episodes of sea-water discoloration reported by the Japan Meteorological Agency (JMA) since August 2022 (Global Volcanism Program, 2023b), we analyzed the event of November 2022, when the Japan Coast Guard (JCG) arranged also a specific aerial overflight over the area.

The JCG documented a bright plume of yellow-white discolored waters originating from the Kaitoku Volcano on 25 November 2022 (Japan Coast Guard (JCG) Volcano Database, 2024). Fig. 8 displays the S2A/MSI discoloration map of 22 November 2022 (i.e., 23 November 2022 10:20 LT) generated using the SDD and SDHD algorithms (Fig. 8c), together with the aerial photos (Fig. 8d, e) obtained by JCG two days after the S2A-MSI acquisition.

From an initial visual overview, spatial features of the discolored plume captured by the aerial overflight are comparable with those visible in the RGB image. Discolored areas identified by the SDD and SDHD algorithms are clearly superimposed with the visible white-green patches in the corresponding true color image (Fig. 8b, c). Also in this case, the SDHD algorithm enables the dome of the plume and the most reflective patches along track to be detected. Furthermore, the SDHD-detected dome of 300 m in diameter coincides with that observed during the aerial overflight two days later (Fig. 8e) (Global Volcanism Program, 2023b). The SDD algorithm, as expected, detected the southwestward portion of the plume, showing less discolored and fragmented features. By looking at the aerial photographs (Fig. 8 d, e), the whitish discolored waters around the Kaitoku Volcano suggests a change in the chemical composition of the seawater compared to the greenish seawater observed close to the Kavachi Volcano (Fig. 5). This analysis

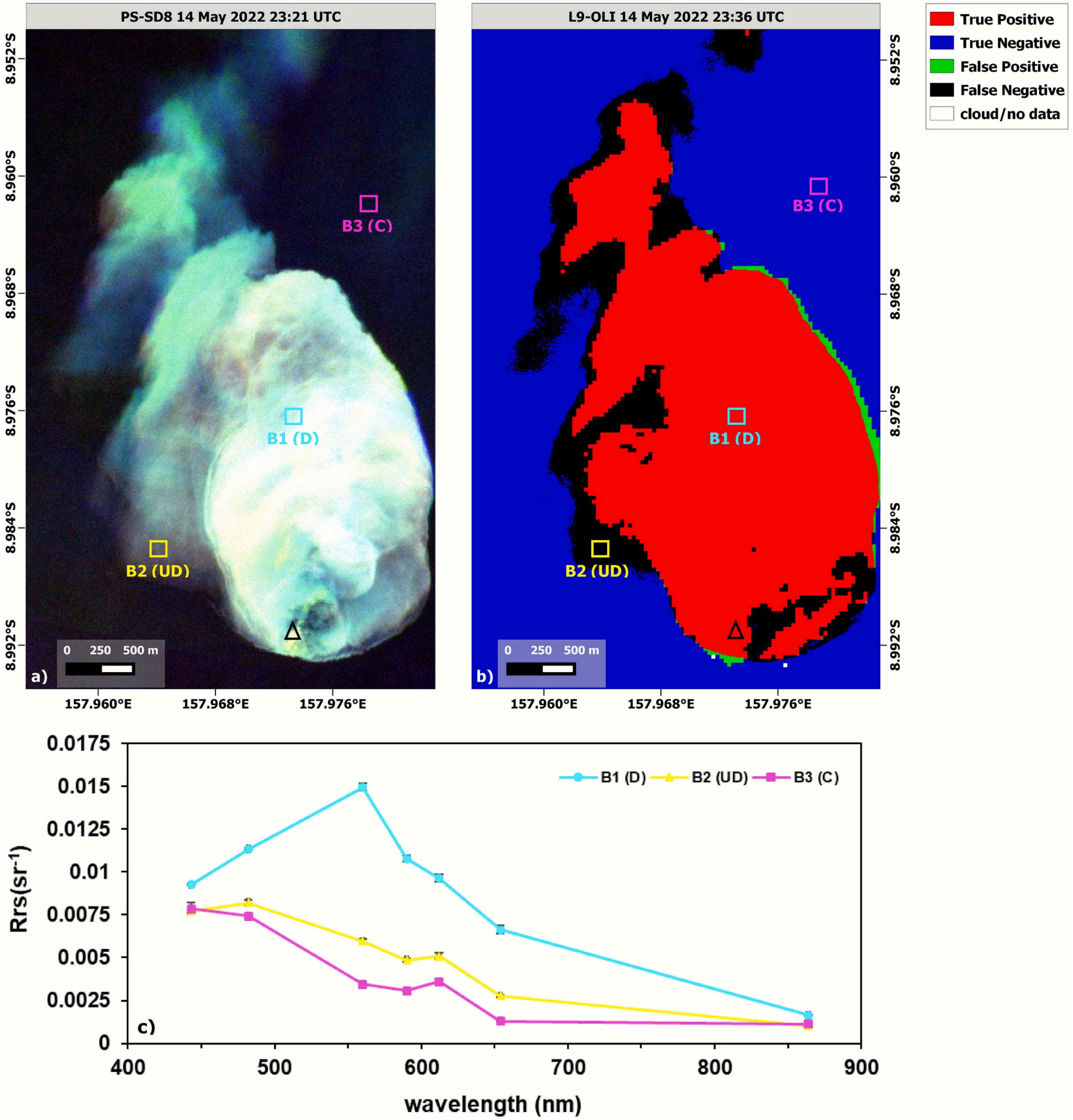

Fig. 7. Validation map from cross-checking. a) PS-SD8 image in true color composite (Red, Green, Blue2) from 14 May 2022. b) L9-OLI validation map from the same test date (acquired 15 min later). c) Rrs(λ) averages and standard deviations (black continuous bars) computed over the three 5 × 5-pixel boxes (i.e., B1(D), B2(UD), B3(C) depicted by the cyan, yellow, and purple squares in the a-b panels, respectively. Validation maps highlight agreement between discolored pixels, TP (red), agreement between other water pixels, TN (blue), disagreements between other water pixels/discolored pixels, FP (green), and disagreements between discolored/other water pixels, FN (black). The location of Kavachi is indicated by the black triangles in (a) and (b). (For interpretation of the references to color in this figure legend, the reader is referred to the web version of this article.)

demonstrates the capacity of the proposed algorithms to detect discolored plumes regardless of the different features of sea-water discoloration (e.g., color shades and/or chemical composition) around submarine volcanoes.

5. Discussion

Monitoring submarine eruptions is not an easy task to achieve by conventional observation methods (e.g., hydro-acoustic, or seismic arrays) considering that eruptions are often short-lived remote events (Mantas et al., 2011). Most of the studies conducted so far by OC data were aimed at timely detecting discolored plumes (or pumice rafts) after

Table 3
Accuracy metrics of the algorithm-derived discoloration mask for the 14 May 2022 test date shown in Fig. 7. CE commission error (overestimation), OE omission error (underestimation), OA overall accuracy and K Cohen's Kappa coefficient.

Satellite-sensor system	CE (%)	OE (%)	OA (%)	K
L9-OLI	2.16	20.91	90.43	0.80

huge submarine eruptions (Fauria et al., 2023; Jutzeler et al., 2020; Shi and Wang, 2011; Whiteside et al., 2023) or studying the biological response of marine ecosystems to volcanic inputs (Barone et al., 2022; Ciancia et al., 2016; Eugenio et al., 2014). Within a scientific framework where the focus is on the post eruptive phase, there is the need to investigate potential precursor signs of submarine volcanic eruptions, such as sea-water discoloration, to support warning and prediction systems (Sakuno et al., 2023).

Among the methods implemented on S2A/B-MSI and Landsat 8/9-OLI data to identify sea-water discoloration (and/or pumice rafts) (Chen et al., 2022; Caballero et al., 2022; Fauria et al., 2023), the Machine Learning (ML) algorithms (e.g., Random Forest) are the most promising, as they can be automated and iteratively-improved (Zheng et al., 2022). Furthermore, deploying these algorithms on the S2A/B and L8/9 L2 reflectance products within the Google Earth Engine (GEE) platform would ensure global scale analysis can be run in a time-effective way without ingesting a large amount of data. However, their operational effectiveness is hampered by a not fully automated classification process that requires manual checks to filter out misclassifications due to sun glint or light cloud cover (Zheng et al., 2022). This limitation underscores the critical need to adopt a water-designed atmospheric correction method to retrieve accurate Rrs(λ) estimations also under contamination effects. The atmospheric correction algorithms (e.g., Sen2cor) on which the GEE-derived L2 reflectance products (S2A/B and L8/9) are based usually fail in optically-complex waters (Kuhn et al., 2019) due to their land-optimized design. Conversely, the ACOLITE-based DSF method is specifically developed for aquatic remote sensing (particularly in turbid waters) and includes options to adjust for sun glint contamination (Vanhellemont, 2019). Its reliability in estimating and correcting this effect allow preventing potential Rrs(λ) overestimates that could falsify the spectral tests (e.g., “Green Threshold”) used for the algorithm configuration. By exploiting the assets of the ACOLITE-DSF tool, we proposed a novel spectrally-derived method to detect and map discolored plumes around submarine volcanoes in oligotrophic oceans, by integrating S2A/B-MSI and L8/9-OLI observations.

5.1. *Reliability, robustness and portability*

Reliability, robustness, and portability are crucial aspects for the development of an automated method for detecting sea-water discoloration around submarine volcanoes. The lack of in-situ data represents a critical issue for the validation of the proposed method. The assumption that satellite data at very high spatial resolution (i.e., PlanetScope) is a proxy of “ground truth” allowed us to overcome this limitation. Very high resolution (VHR), in fact, may allow for a better identification (and interpretation) of the observed discolored plumes and may represent a valid source for their validation. Although it is not always possible, this approach can be largely used, due to the increasing availability of VHR satellite data at low or even no cost (Lesiv et al., 2018).

Another relevant aspect that deserves to be thoroughly evaluated is whether a discolored plume of volcanic origin can be distinguished from a biological one (e.g., phytoplankton bloom). Since we did not find any information about the occurrence of a phytoplankton bloom within the study area from previous studies, we performed a confutation analysis

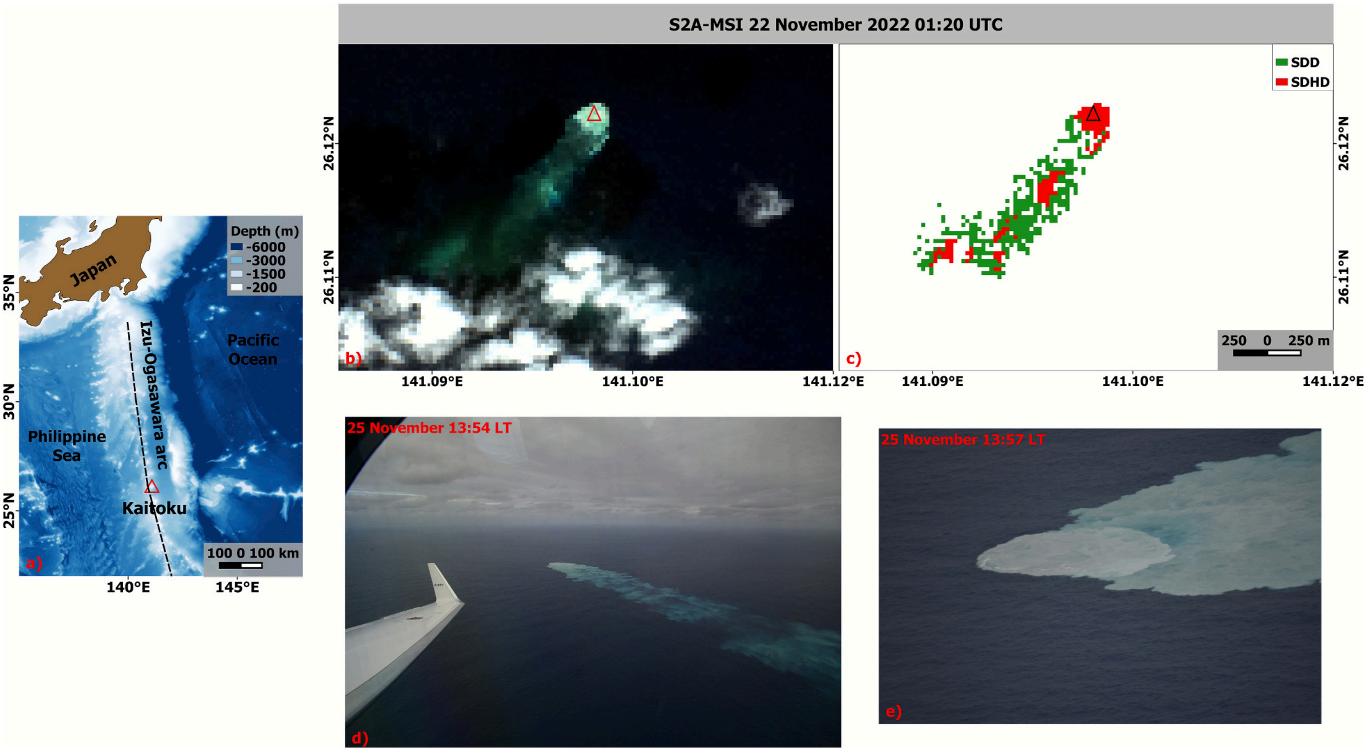

Fig. 8. Algorithm exportability. a) Location of the Kaitoku Volcano (Izu-Ogasawara arc, Northwest Pacific Ocean) over the bathymetric data obtained from the GEBCO (GEBCO Catalogue, 2024). b) S2A-MSI image in true color composite (Red, Green, Blue2) on 22 November 2022. c) Discoloration map derived by the SDD (green) and SDHD (red) algorithms on 22 November 2022 (23 November 2022 10:20 LT). d, e) Aerial photos acquired (from the west and north, respectively) by the Japan Coast Guard on 25 November 2022 (Japan Coast Guard (JCG) Volcano Database, 2024). The location of Kaitoku is depicted by the red triangles in (a) and (b) and the black triangle in (c). (For interpretation of the references to color in this figure legend, the reader is referred to the web version of this article.)

by investigating an anomalous bloom over the Southern Pacific Ocean (similar oligotrophic waters) to assess the robustness of the proposed discoloration method toward such kind of possible "look-alike" (i.e., similar effects originating from different, not volcanic, causes). The investigated phytoplankton bloom was likely triggered by the severe 2019–2020 Australian wildfires and started around October 2019 with a peak in January 2020 (Tang et al., 2021). In this case, chlorophyll-a (chl-a) reached concentrations never observed in a 22-year satellite time series from the ESA's Ocean Colour Climate Change Initiative (ESA OC-CCI) (Tang et al., 2021). For the confutation analysis, we considered the Level 3 monthly chl-a product (version 6) and the corresponding Rrs(λ) data at 443, 490, 560 and 665 nm for January 2020 at 4 km spatial resolution from the ESA OC-CCI database (ESA OC-CCI Dataset, 2025). In this context, we evaluated the reliability of two spectral tests in avoiding detection of potential discolored pixels due to a phytoplankton bloom in oligotrophic oceans. Fig. 9 shows the variability of the "Blue ratio" and Rrs(Green) along a transect (of about 5000 km) crossing the monthly chl-a map for January 2020 over the Southern Pacific area of interest.

Fig. 9 shows that most of the area investigated was affected by an anomalous phytoplankton bloom, since chl-a reaches concentrations up to 0.6 mg/m^3, significantly higher than the climatological value of 0.08

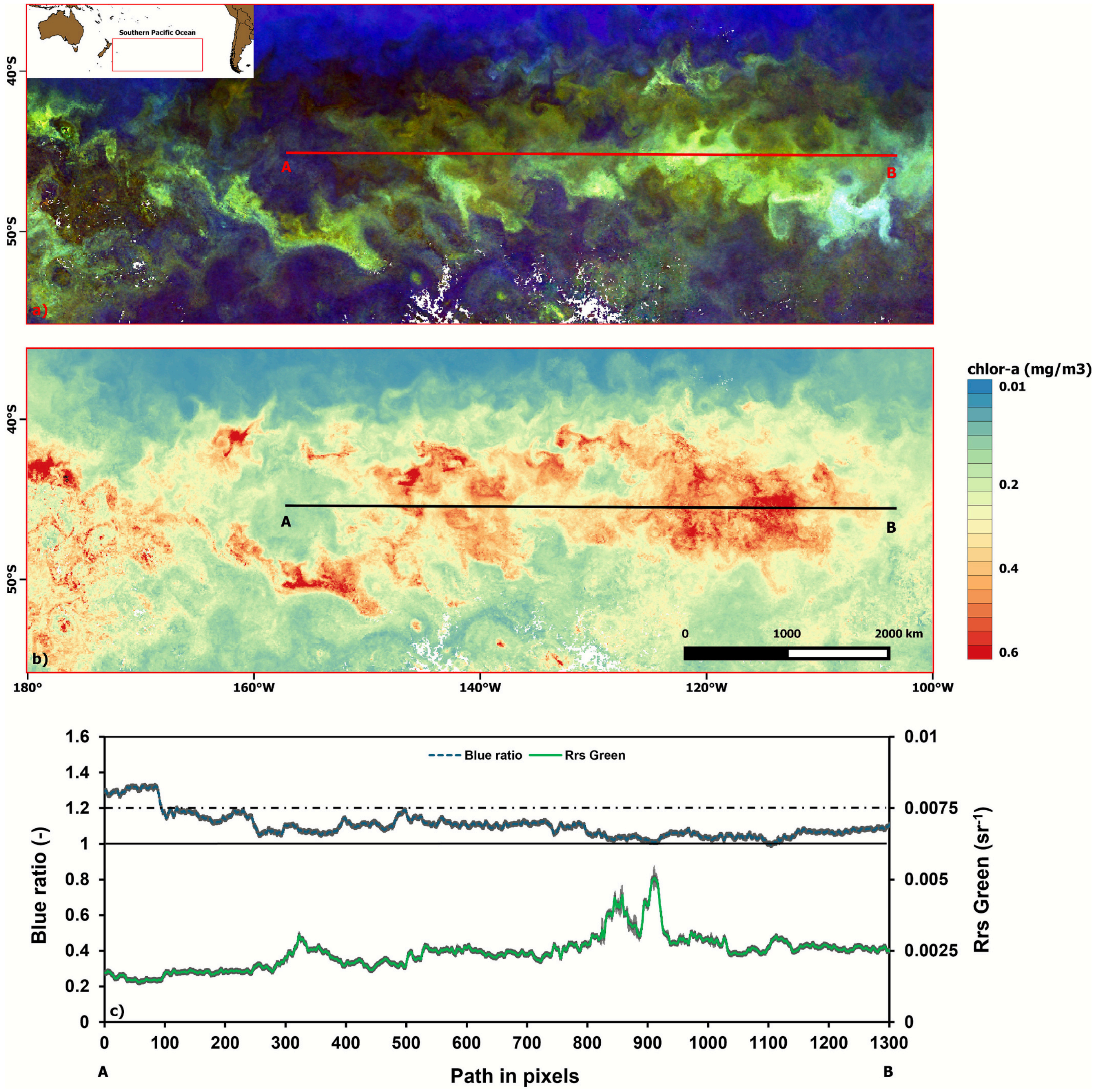

Fig. 9. Confutation analysis. a) Monthly RGB (665, 560, 443) map for January 2020 over the Southern Pacific subset delimited by the red rectangle on the inset in the top left. b) Monthly Chl-a map for January 2020 over the same study area as a). c) Profiles of Blue ratio (Rrs(443)/Rrs(490)) and Rrs(Green) along the A-B transect. The continuous and dashed black lines are the reference value for the Blue ratio and the threshold value (0.0075 sr^{-1}) for Rrs(Green), respectively. (For interpretation of the references to color in this figure legend, the reader is referred to the web version of this article.)

mg/m^3 for this area (Tang et al., 2021). Along the 5000 km transect (A-B) crossing the main chl-a patterns, the Blue ratio is about 1.3 close to A and then it ranges between 1.2 and 1 (Fig. 9b). Since the Blue ratio is always above the threshold value of 1, the SDD or SDHD would not have detected any discolored pixels, despite such an extreme bloom for oligotrophic waters.

The Rrs(Green) is almost always around 0.0025–0.003 sr^{-1} except for a peak of ~0.005 sr^{-1} corresponding to the highest chl-a values (0.6 mg/m^3), but it always remains well below the threshold value of 0.0075 sr^{-1} (Fig. 9b). The adoption of the Rrs(Green) threshold, specifically designed to characterize ash-laden waters, would enable the possible discolored waters of biological origin to be excluded from detection. Thus, these analyses indicate that the proposed method (integrating information from SDD and SDHD algorithms) can discriminate discolored waters of biological origin from those associated with underwater volcanic activity in oligotrophic water conditions.

5.2. *Findings and future perspectives*

The interpretation of the detected discolored plumes is another relevant aspect that should be considered. In this work, the SDD and SDHD showed a good capacity to detect pixels with different discoloration intensities around the Kavachi Volcano. In more detail, the SDHD was effective for the plume cores with higher intensity of discoloration ranging from green to yellow-brown close to the volcano. The SDD allowed for the detection of larger and less discolored areas, with prevailing greenish shades that shifted to green-blue further away. The predominant color of a volcanic discolored plume may reveal information on the main substances released, specifically those based on iron (Fe), aluminum (Al), and silicon (Si) (Nogami et al., 1993; Onda, 2003; Sakuno et al., 2023; Urai and Machida, 2005). A higher proportion of Fe usually produces mostly green shades and/or yellow brown colors, whereas a higher proportion of Al or Si generates whitish tones of color (Sakuno, 2021). Considering the prevalent green shades (with some yellow-to-brown transitions) of the observed discolored plumes around the Kavachi Volcano, it is reasonable to assume a predominance of iron released by the underwater volcanic activity. However, these assumptions should be supported by physical-chemical analysis of sub-surface water samples to measure changes in water properties due to inorganic ash particles and emitted gases from the volcano (Olgun et al., 2013; Matsuo et al., 2025).

Turning to the analysis of accuracy, the single discoloration algorithm, including both the SDD and SDHD configurations, reliably identified truly discolored pixels considering the negligible numbers of false detections (with CEs around 2%). Despite its robustness, the algorithm slightly lacks sensitivity and tends to underestimate the less discolored plume regions. Using a threshold approach (i.e., in the Green band) may reduce sensitivity, resulting in the failure to identify truly discolored pixels in the most distal part of the plume and/or the core edges.

However, the method's capability to minimize false detections plays a key role in an early warning system for monitoring submarine volcanic activity. Furthermore, the assessed exportability of the method in areas with a different sea-water discoloration (e.g., color shades and/or chemical composition) is another crucial asset for its operational usage. National environmental (or meteorological) agencies could exploit these strengths to arrange different early warning levels for possible subaerial eruptions by monitoring discolored plumes around submarine volcanoes. Increases in intensity and spatial extent of discolored plumes due to a higher release of volcanic matter may heighten the probability of an impending subaerial eruption. To this aim, the Japan Meteorological Agency (JMA) established two-level of alerts (i.e., “Volcanic Forecast” and “Volcanic Warning, Sea Area”) for submarine volcanoes based on the observations/photos of discolored plumes provided by the Japan Coast Guard (JCG) during ad-hoc monitoring overflights (Global Volcanism Program, 2025). It is therefore of paramount importance to develop systems capable of providing timely and reliable information about seawater discoloration before submarine eruptions transition to subaerial eruptions.

In this direction, both the OLI and MSI sensors open new perspectives to identify and track fine-scale discolored features drifting from volcanoes. Moreover, their combined use may enable the monitoring of discolored plumes at unprecedented rates, with a potential revisit time of 2–3 days on a global scale (Pahlevan et al., 2017). The detected discolored plume around the Kaitoku Volcano at the end of November 2022 represents an example of the method capability in supporting the monitoring actions by satellite data integration.

From a future perspective, it would be worth testing the applicability of the method also in higher productivity oceans and shallow coastal waters, by improving the SDD/SDHD algorithm (e.g., with specific spectral test and/or thresholds). For instance, the adopted “Blue ratio” test could result ineffective in discriminating volcano-ash pixels from shallow waters where the Rrs(Blue1) is generally lower than Rrs(Blue2) due to sea-bottom contribution (Arabi et al., 2020). Furthermore, there would need to be a better characterization of underwater volcanic activity by providing satellite estimations of water quality indicators, such as turbidity (or suspended matter concentrations), k_d (490) or $b_{bp}(\lambda)$, on the SDD/SDHD-detected discolored plumes. These parameters could be used to perform correlation analyses with seismic array data to establish potential relationships for predictive purposes. For instance, it is reasonable to assume that the largest extent of SDHD-detected plume and/or the corresponding maximum value of turbidity could be associated with the highest seismic activity recorded within a certain time lag. However, correlating sea-discoloration parameters with data from seismic arrays requires daily satellite revisits. The exportability of the proposed method on Ocean Land Colour Instrument (OLCI), onboard Sentinel 3 (S3) satellite-platform, could minimize satellite acquisition gaps, improving the temporal coverage.

An integrated multi-sensor satellite system, exploiting S2A/B-MSI, L8/9-OLI and S3-OLCI observations, will enable the development of an automated tool for detecting, mapping, and monitoring sea-water discolored plumes addressing the observational gaps in the investigation of submarine volcanoes.

6. Conclusions

In this work, we proposed a novel spectrally-derived method to detect and map discolored plumes around submarine volcanoes in oligotrophic oceans by integrating Sentinel 2 A/B-MSI and Landsat 8/9-OLI data.

We investigated 20 discoloration episodes that occurred in 2022 around the Kavachi Volcano (Solomon Islands, Southwest Pacific Ocean), to characterize the reference spectral shapes (i.e., Rrs(λ)) of clear, discolored and highly discolored waters. Based on differences between these reference Rrs(λ), we defined a set of spectral tests/thresholds to develop a method to identify discolored plumes of volcanic origin. To account for different discoloration intensities, we proposed two algorithm configurations, namely the SDD and the SDHD. The SDHD usually enabled the identification of the plume cores of higher intensity of discoloration, while SDD performed an effective detection of larger and less discolored areas in the more distal parts of the plume.

The developed method, combining the two discoloration algorithms, exhibited satisfactory metrics thus recording OAs close to 90%, CEs not exceeding 1% and K values of about 0.8 for both the single and integrated (multi-sensor) configuration. Despite OEs ranging from 18 to 20%, which may be ascribed to a lower sensitivity over plume edges (or transition zones), the very low CEs (around 2%) demonstrate the high reliability level of this method in mapping discolored waters associated with the submarine volcanic activity.

The proven exportability of the method in other areas, such as Kaitoku, confirms its capability in detecting underwater volcanic activity regardless of different features of sea-water discoloration (e.g., color shades and/or chemical composition).

The developed satellite sea-water discoloration method may, then, represent a valid tool to support the operational monitoring of submarine volcanoes. In the framework of early warning systems, it will be capable of providing continuous and timely information about sea-water discoloration before submarine eruptions transition to subaerial eruptions.

CRediT authorship contribution statement

Emanuele Ciancia: Writing – original draft, Methodology, Investigation, Data curation. **Francesco Marchese:** Supervision, Conceptualization. **Giuseppe Mazzeo:** Visualization, Validation, Software. **Simon Plank:** Validation, Investigation, Formal analysis. **Nicola Pergola:** Supervision, Formal analysis.

Declaration of competing interest

The authors declare that they have no known competing financial interests or personal relationships that could have appeared to influence the work reported in this paper.

Acknowledgments

The aerial photographs (public domain) were used with the permission of the Japan Coast Guard (JCG).

Appendix A. Supplementary data

Supplementary data to this article can be found online at https://doi.org/10.1016/j.marpolbul.2026.119266.

Data availability

Data will be made available on request.

References

ACOLITE software, 2024. https://odnature.naturalsciences.be/remsem/acolite-forum (accessed 24 April 2024).

Arabi, B., Salama, M.S., van der Wal, D., Pitarch, J., Verhoef, W., 2020. The impact of sea bottom effects on the retrieval of water constituent concentrations from MERIS and OLCI images in shallow tidal waters supported by radiative transfer modeling. Remote Sens. Environ. 237, 111596.

Baker, E.T., Massoth, G.J., de Ronde, C.E.J., Lupton, J.E., McInnes, B.I.A., 2002. Observations and sampling of an ongoing subsurface eruption of Kavachi volcano, Solomon Islands, May 2000. Geology 30, 975–978.

Baker, E.T., Chadwick Jr., W.W., Cowen, J.P., Dziak, R.P., Rubin, K.H., Fornari, D.J., 2012. Hydrothermal discharge during submarine eruptions: the importance of detection, response, and new technology. Oceanography 25 (1).

Bali, H., Gupta, A.K., Mohan, K., Thirumalai, K., Tiwari, S.K., Panigrahi, M.K., 2020. Evolution of the oligotrophic West Pacific warm pool during the Pliocene-Pleistocene boundary. Paleoceanogr. Paleoclimatol. 35 (11) e2020PA003875.

Barone, B., Letelier, R.M., Rubin, K.H., Karl, D.M., 2022. Satellite detection of a massive phytoplankton bloom following the 2022 submarine eruption of the Hunga Tonga-Hunga Ha'apai Volcano. Geophys. Res. Lett. 49 (17) e2022GL099293.

Caballero, I., Román, A., Tovar-Sánchez, A., Navarro, G., 2022. Water quality monitoring with Sentinel-2 and Landsat-8 satellites during the 2021 volcanic eruption in La Palma (Canary Islands). Sci. Total Environ. 822, 153433.

Chen, X., Sun, S., Zhao, J., Ai, B., 2022. Spectral discrimination of pumice rafts in optical MSI imagery. Remote Sens. 14 (22), 5854.

Ciancia, E., Magalhães Loureiro, C., Mendonça, A., Coviello, I., Di Polito, C., Lacava, T., Pergola, N., Satriano, V., Tramutoli, V., Martins, A., 2016. On the potential of an RST-based analysis of the MODIS-derived chl-a product over Condor seamount and surrounding areas (Azores, NE Atlantic). Ocean Dyn. 66 (9), 1165–1180.

Ciancia, E., Campanelli, A., Lacava, T., Palombo, A., Pascucci, S., Pergola, N., Pignatti, S., Satriano, V., Tramutoli, V., 2020. Modeling and multi-temporal characterization of total suspended matter by the combined use of Sentinel 2-MSI and Landsat 8-OLI data: the Pertusillo Lake case study (Italy). Remote Sens. 12 (13), 2147.

Ciancia, E., Campanelli, A., Colonna, R., Palombo, A., Pascucci, S., Pignatti, S., Pergola, N., 2023. Improving colored dissolved organic matter (CDOM) retrievals by Sentinel2-MSI data through a total suspended matter (TSM)-Driven classification: the case of Pertusillo lake (Southern Italy). Remote Sens. 15 (24), 5718.

Coca, J., Ohde, T., Redondo, A., García-Weil, L., Santana-Casiano, M., González-Dávila, M., Aristegui, J., Fraile-Nuez, E., Ramos, A.G., 2014. Remote sensing of the El Hierro submarine volcanic eruption plume. Int. J. Remote Sens. 35 (17), 6573–6598.

Coluzzi, R., Imbrenda, V., Lanfredi, M., Simoniello, T., 2018. A first assessment of the Sentinel-2 Level 1-C cloud mask product to support informed surface analyses. Remote Sens. Environ. 217, 426–443.

Coluzzi, R., Perrone, A., Samela, C., Imbrenda, V., Manfreda, S., Pace, L., Lanfredi, M., 2025. Rapid landslide detection from free optical satellite imagery using a robust change detection technique. Sci. Rep. 15 (1), 4697.

Congalton, R.G., 1991. A review of assessing the accuracy of classifications of remotely sensed data. Remote Sens. Environ. 37 (1), 35–46.

Copernicus browser, 2024. https://browser.dataspace.copernicus.eu. (Accessed 18 May 2024).

Di Polito, C., Ciancia, E., Coviello, I., Doxaran, D., Lacava, T., Pergola, N., Satriano, V., Tramutoli, V., 2016. On the potential of robust satellite techniques approach for SPM monitoring in coastal waters: implementation and application over the Basilicata Ionian coastal waters using MODIS-Aqua. Remote Sens. 8 (11), 922.

Doxaran, D., Froidefond, J., Lavender, S., Castaing, P., 2002. Spectral signature of highly turbid waters application with SPOT data to quantify suspended particulate matter concentrations. Remote Sens. Environ. 81, 149–161.

Dziak, R.P., Hammond, S.R., Fox, C.G., 2011. A 20-year hydroacoustic time series of seismic and volcanic events in the northeast Pacific Ocean. Oceanography 24, 280–293.

ESA OC-CCI Dataset, 2025. https://esa-oceancolour-cci.org/. (Accessed 28 March 2025).

Eugenio, F., Martin, J., Marcello, J., Fraile-Nuez, E., 2014. Environmental monitoring of El Hierro Island submarine volcano, by combining low and high resolution satellite imagery. Int. J. Appl. Earth Obs. Geoinf. 29, 53–66.

Falconieri, A., Marchese, F., Ciancia, E., Genzano, N., Mazzeo, G., Pietrapertosa, C., Pergola, N., Plank, S., Filizzola, C., 2025. Exploring the potential of a normalized hotspot index in supporting the monitoring of active volcanoes through Sea and Land Surface Temperature Radiometer Shortwave Infrared (SLSTR SWIR) data. Sensors (Basel, Switzerland) 25 (6), 1658.

Fauria, K.E., Jutzeler, M., Mittal, T., Gupta, A.K., Kelly, L.J., Rausch, J., Bennartz, R., Delbridge, B., Retailleau, L., 2023. Simultaneous creation of a large vapor plume and pumice raft by the 2021 Fukutoku-Oka-no-Ba shallow submarine eruption. Earth Planet. Sci. Lett. 609, 118076.

Fraile-Nuez, E., González-Dávila, M., Santana-Casiano, J.M., Arístegui, J., Alonso-González, I.J., Hernández-León, S., Blanco, M.J., Rodriguez-Santana, A., Hernandez-Guerra, A., Gelado-Caballero, M.D., Eugenio, F., Marcello, J., de Armas, D., Dominguez-Yanes, J.F., Montero, M.F., Laetsch, D.R., Velez-Belchi, P., Ramos, A., Ariza, A.V., Comas-Rodriguez, I., Benítez-Barrios, V.M., 2012. The submarine volcano eruption at the island of El Hierro: physical-chemical perturbation and biological response. Sci. Rep. 2 (1), 486.

GEBCO Catalogue, 2024. https://www.bodc.ac.uk/data/hosted_data_systems/gebco_gridded_bathymetry_data. (Accessed 13 March 2025).

GeoMapApp tool, 2009. https://www.geomapapp.org. (Accessed 18 December 2025).

Gernez, P., Zoffoli, M.L., Lacour, T., Fariñas, T.H., Navarro, G., Caballero, I., Harmel, T., 2023. The many shades of red tides: Sentinel-2 optical types of highly-concentrated harmful algal blooms. Remote Sens. Environ. 287, 113486.

Global Volcanism Program, 1976. Report on Kavachi (Solomon Islands). In: Squires, D. (Ed.), Nat. Sci. Event Bull, 1:12. Smithsonian Institution. https://doi.org/10.5479/si.GVP.NSEB197609-255060.

Global Volcanism Program, 1978. Report on Kavachi (Solomon Islands). In: Squires, D. (Ed.), Sci. Event Alert Netw. Bull, 3:7. Smithsonian Institution. https://doi.org/10.5479/si.GVP.SEAN197807-255060.

Global Volcanism Program, 1991. Report on Kavachi (Solomon Islands). In: McClelland, L. (Ed.), Bull. of the Glob. Volcan. Netw, 16:4. Smithsonian Institution. https://doi.org/10.5479/si.GVP.BGVN199104-255060.

Global Volcanism Program, 2000. Report on Kavachi (Solomon Islands). In: Wunderman, R. (Ed.), Bull. of the Glob. Volcan. Netw, 25:4. Smithsonian Institution. https://doi.org/10.5479/si.GVP.BGVN200004-255060.

Global Volcanism Program, 2005. Report on Kavachi (Solomon Islands). In: Wunderman, R. (Ed.), Bull. of the Glob. Volcan. Netw, 30:3. Smithsonian Institution. https://doi.org/10.5479/si.GVP.BGVN200503-255060.

Global Volcanism Program, 2017. Report on Kavachi (Solomon Islands). In: Venzke, E. (Ed.), Bull. of the Glob. Volcan. Netw, 42:3. Smithsonian Institution. https://doi.org/10.5479/si.GVP.BGVN201703-255060.

Global Volcanism Program, 2021. Report on Kavachi (Solomon Islands). In: Bennis, K.L., Andrews, B. (Eds.), Bull. of the Glob. Volcan. Netw, 46:11. Smithsonian Institution. https://doi.org/10.5479/si.GVP.BGVN202111-255060.

Global Volcanism Program, 2022. Report on Kavachi (Solomon Islands). In: Bennis, K.L., Venzke, E. (Eds.), Bull. of the Glob. Volcan. Netw, 47:8. Smithsonian Institution.

Global Volcanism Program, 2023a. Report on Kavachi (Solomon Islands). In: Bennis, K. L., Venzke, E. (Eds.), Bull. of the Glob. Volcan. Netw, 48:3. Smithsonian Institution.

Global Volcanism Program, 2023b. Report on Kaitoku Seamount (Japan). In: Bennis, K. L., Venzke, E. (Eds.), Bull.of the Glob. Volcan. Netw, 48:2. Smithsonian Institution. https://doi.org/10.5479/si.GVP.BGVN202302-284100.

Global Volcanism Program, 2025. Report on Kaitoku Seamount (Japan). In: Sennert, S. (Ed.), Wkly. Volc. Act. Rep., 26 February-4 March 2025. Smithsonian Institution and US Geological Survey.

González-Vega, A., Fraile-Nuez, E., Santana-Casiano, J.M., González-Dávila, M., Escánez-Pérez, J., Gómez-Ballesteros, M., Olvido, T., Arrieta, J.M., 2020. Significant release of dissolved inorganic nutrients from the shallow submarine volcano Tagoro (Canary Islands) based on seven-year monitoring. Front. Mar. Sci. 6, 829.

Green, D.N., Evers, L.G., Fee, D., Matoza, R.S., Snellen, M., Smets, P., Simons, D., 2013. Hydroacoustic, infrasonic and seismic monitoring of the submarine eruptive activity and sub-aerial plume generation at South Sarigan, May 2010. J. Volcanol. Geotherm. Res. 257, 31–43.

Hu, C., Lee, Z., Franz, B., 2012. Chlorophyll algorithms for oligotrophic oceans: a novel approach based on three-band reflectance difference. J. Geophys. Res. Oceans 117 (C1).

Japan Coast Guard (JCG) Volcano Database, 2024. https://www1.kaiho.mlit.go.jp/kaiikiDB/kaiyo20-2.htm. (Accessed 23 November 2024).

Jiang, D., Matsushita, B., Pahlevan, N., Gurlin, D., Fichot, C.G., Harringmeyer, J., Sent, J., Brito, A.C., Brotas, V., Werther, M., Mascarenas, V., Blake, M., Hunter, P., Tyler, A., Spyrakos, E., 2023. Estimating the concentration of total suspended solids in inland and coastal waters from Sentinel-2 MSI: a semi-analytical approach. ISPRS J. Photogramm. Remote Sens. 204, 362–377.

Jiang, D., Matsushita, B., Pahlevan, N., Gurlin, D., Lehmann, M.K., Fichot, C.G., Schalles, J., Loisel, H., Binding, C., Zhang, Y., Alikas, K., Kangro, K., Uusoue, M., Ondrusek, M., Greb, S., Moses, W., Lohrenz, S., O'Donnell, D., 2021. Remotely estimating total suspended solids concentration in clear to extremely turbid waters using a novel semi-analytical method. Remote Sens. Environ. 258, 112386.

Jutzeler, M., Marsh, R., van Sebille, E., Mittal, T., Carey, R.J., Fauria, K.E., Manga, M., McPhie, J., 2020. Ongoing dispersal of the 7 August 2019 pumice raft from the Tonga Arc in the Southwestern Pacific Ocean. Geophys. Res. Lett. 47, e1701121.

Kelly, L.J., Fauria, K.E., Manga, M., Cronin, S.J., Latu'ila, F.H., Paredes-Mariño, J., Mittal, T., Bennartz, R., 2024. Airfall volume of the 15 January 2022 eruption of Hunga volcano estimated from ocean color changes. Bull. Volcanol. 86 (6), 59.

Kuhn, C., de Matos Valerio, A., Ward, N., Loken, L., Sawakuchi, H.O., Kampel, M., Richey, J., Stadler, P., Crawford, J., Striegl, R., Vermote, E., Pahlevan, N., Butman, D., 2019. Performance of Landsat-8 and Sentinel-2 surface reflectance products for river remote sensing retrievals of chlorophyll-a and turbidity. Remote Sens. Environ. 224, 104–118.

Lesiv, M., See, L., Laso Bayas, J.C., Sturn, T., Schepaschenko, D., Karner, M., Moorthy, I., McCallum, I., Fritz, S., 2018. Characterizing the spatial and temporal availability of very high resolution satellite imagery in Google Earth and Microsoft Bing Maps as a source of reference data. Land 7 (4), 118.

Mantas, V.M., Pereira, A.J.S.C., Morais, P.V., 2011. Plumes of discolored water of volcanic origin and possible implications for algal communities. The case of the Home Reef eruption of 2006 (Tonga, Southwest Pacific Ocean). Remote Sens. Environ. 115 (6), 1341–1352.

Matsuo, T., Ito-Miwa, K., Hoshino, Y., Fujii, Y.I., Kanno, S., Fujimoto, K.J., Tsuji, R., Takeda, S., Onami, C., Arai, C., Yoshiyama, Y., Mino, Y., Kato, Y., Yanai, T., Fujita, Y., Masuda, S., Kakegawa, T., Miyashita, H., 2025. Archaean green-light environments drove the evolution of cyanobacteria's light-harvesting system. Nat. Ecol. Evol. 1–14.

Mélin, F., Sclep, G., Jackson, T., Sathyendranath, S., 2016. Uncertainty estimates of remote sensing reflectance derived from comparison of ocean color satellite data sets. Remote Sens. Environ. 177, 107–124.

Mitchell, N., 2012. Submarine volcanism: hot, cracking rocks deep down. Nat. Geosci. 5 (7), 444–445. https://doi.org/10.1038/ngeo1505.

Nogami, K., Yoshida, M., Ossaka, J., 1993. Chemical composition of discolored seawater around Satsuma-Iwojima, Kagoshima, Japan. Bull. Volcanol. Soc. Jpn. Series 2 (38), 71–77.

Olgun, N., Duggen, S., Langmann, B., Hort, M., Waythomas, C.F., Hoffmann, L., Croot, P., 2013. Geochemical evidence of oceanic iron fertilization by the Kasatochi volcanic eruption in 2008 and the potential impacts on Pacific sockeye salmon. Mar. Ecol. Prog. Ser. 488, 81–88.

O'Malley, R.T., Behrenfeld, M.J., Westberry, T.K., Milligan, A.J., Reese, D.C., Halsey, K. H., 2014. Improbability mapping: a metric for satellite-detection of submarine volcanic eruptions. Remote Sens. Environ. 140, 596–603.

Onda, S., 2003. A colorimetric and geochemical study of the coloration factor of hyper-acid active crater lakes. Jpn. J. Limnol. 64, 1–10.

Page, B.P., Olmanson, L.G., Mishra, D.R., 2019. A harmonized image processing workflow using Sentinel-2/MSI and Landsat-8/OLI for mapping water clarity in optically variable lake systems. Remote Sens. Environ. 231, 111284.

Pahlevan, N., Chittimalli, S.K., Balasubramanian, S.V., Vellucci, V., 2019. Sentinel-2/Landsat-8 product consistency and implications for monitoring aquatic systems. Remote Sens. Environ. 220, 19–29.

Pahlevan, N., Sarkar, S., Franz, B.A., Balasubramanian, S.V., He, J., 2017. Sentinel-2 MultiSpectral Instrument (MSI) data processing for aquatic science applications: demonstrations and validations. Remote Sens. Environ. 201, 47–56.

Phillips, B.T., Dunbabin, M., Henning, B., Howell, C., DeCiccio, A., Flinders, A., Kelley, K. A., Scott, J.J., Albert, S., Carey, S., Tsadok, R., Grinham, A., 2016. Exploring the "Sharkcano": biogeochemical observations of the Kavachi submarine volcano (Solomon Islands). Oceanography 29 (4).

Planet Developer Center, 2024. https://developers.planet.com/. (Accessed 20 June 2024).

Plank, S., Ciancia, E., Genzano, N., Falconieri, A., Martinis, S., Taubenböck, H., Pergola, N., Marchese, F., 2025. The evolution of the 2022–2024 eruption at Home Reef, Tonga, analyzed from space shows vent migration due to erosion. Sci. Rep. 15 (1), 11508.

Qi, L., Hu, C., Mikelsons, K., Wang, M., Lance, V., Sun, S., Van der Zande, D., 2020. In search of floating algae and other organisms in global oceans and lakes. Remote Sens. Environ. 239, 111659.

Rubin, K.H., Soule, S.A., Chadwick Jr., W.W., Fornari, D.J., Clague, D.A., Embley, R.W., Baker, E.T., Perfit, M.R., Caress, D.W., Dziak, R., 2012. Volcanic eruptions in the deep sea. Oceanography 25 (1), 142–157. https://doi.org/10.5670/oceanog.2012.12.

Ryan, W.B.F., Carbotte, S.M., Coplan, J.O., O'Hara, S., Melkonian, A., Arko, R., Weissel, R.A., Ferrini, V., Goodwillie, A., Nitsche, F., Bonczkowski, J., Zemsky, R., 2009. Global multi-resolution topography synthesis. Geochem. Geophys. Geosyst. 10, Q03014. https://doi.org/10.1029/2008GC002332.

Sakuno, Y., 2021. Trial of chemical composition estimation related to submarine volcano activity using discolored seawater color data obtained from GCOM-C SGLI. A case study of Nishinoshima Island, Japan, in 2020. Water 13 (8), 1100.

Sakuno, Y., Hirao, S., Taniguchi, N., 2023. Quantitatively mapping discolored seawater around submarine volcanoes using satellite GCOM-C SGLI data: a case study of the Krakatau Eruption in Indonesia in December 2018. GeoHazards 4 (2), 107–120.

Satriano, V., Ciancia, E., Pergola, N., Tramutoli, V., 2024. A first extension of the robust satellite technique RST-FLOOD to Sentinel-2 data for the mapping of flooded areas: the case of the Emilia Romagna (Italy) 2023 Event. Remote Sens. 16 (18), 3450.

Schlindwein, V., Muller, C., Jokat, W., 2005. Seismoacoustic evidence for volcanic activity on the ultraslow-spreading Gakkel Ridge, Arctic Ocean. Geophys. Res. Lett. 32, L18306.

Shi, W., Wang, M., 2011. Satellite observations of environmental changes from the Tonga volcano eruption in the southern tropical Pacific. Int. J. Remote Sens. 32 (20), 5785–5796.

Spyrakos, E., Odonnell, R., Hunter, P.D., Miller, C., Scott, M., Simis, S.G., Tyler, A.N., 2018. Optical types of inland and coastal waters. Limnol. Oceanogr. 63, 846–870.

Tang, W., Llort, J., Weis, J., Perron, M.M., Basart, S., Li, Z., Sathyendranath, S., Jackson, T., Sanz Rodriguez, E., Proemse, B.C., Bowie, A.R., Schallenberg, C., Strutton, P.G., Matear, R., Cassar, N., 2021. Widespread phytoplankton blooms triggered by 2019–2020 Australian wildfires. Nature 597 (7876), 370–375.

Tepp, G., Dziak, R.P., 2021. The seismo-acoustics of submarine volcanic eruptions. J. Geophys. Res. Solid Earth 126 (4) e2020JB020912.

United States Geological Survey (USGS) Web Portal, 2024. https://earthexplorer.usgs.gov. (Accessed 19 July 2024).

Urai, M., 2014. Time series analysis of discolored seawater reflectance observed by Advanced Visible and Near Infrared Radiometer type 2 (AVNIR-2) at Fukutoku-Okonaba submarine volcano, Japan. J. Volcanol. Geotherm. Res. 269, 23–27.

Urai, M., Machida, S., 2005. Discolored seawater detection using ASTER reflectance products: a case study of Satsuma-Iwojima, Japan. Remote Sens. Environ. 99 (1–2), 95–104.

Vanhellemont, Q., 2019. Adaptation of the dark spectrum fitting atmospheric correction for aquatic applications of the Landsat and Sentinel-2 Archives. Remote Sens. Environ. 225, 175–192.

Vanhellemont, Q., 2020. Sensitivity analysis of the dark spectrum fitting atmospheric correction for metre-and decametre-scale satellite imagery using autonomous hyperspectral radiometry. Opt. Express 28 (20), 29948–29965.

Vanhellemont, Q., 2023. Evaluation of eight band SuperDove imagery for aquatic applications. Opt. Express 31 (9), 13851–13874.

Vanhellemont, Q., Ruddick, K., 2018. Atmospheric correction of metre-scale optical satellite data for inland and coastal water applications. Remote Sens. Environ. 216, 586–597.

Whiteside, A., Dupouy, C., Singh, A., Frouin, R., Menkes, C., Lefèvre, J., 2021. Automatic detection of optical signatures within and around floating Tonga-Fiji pumice rafts using MODIS, VIIRS, and OLCI satellite sensors. Remote Sens. 13 (3), 501.

Whiteside, A., Dupouy, C., Singh, A., Bani, P., Tan, J., Frouin, R., 2023. Impact of ashes from the 2022 Tonga volcanic eruption on satellite ocean color signatures. Front. Mar. Sci. 9, 1028022.

Zheng, M., Mittal, T., Fauria, K.E., Subramaniam, A., Jutzeler, M., 2022. Pumice raft detection using machine-learning on multispectral satellite imagery. Front. Earth Sci. 10, 838532.